

ASHLEY: A new empirical model for the high-latitude electron precipitation and electric field

Qingyu Zhu¹, Yue Deng¹, Astrid Maute², Liam Kilcommons³, Delores Knipp³, and Marc Hairston⁴

¹University of Texas at Arlington

²National Center for Atmosphere Research

³University of Colorado Boulder

⁴University of Texas at Dallas

November 24, 2022

Abstract

In this study, a new high-latitude empirical model is introduced, named for Auroral energy Spectrum and High-Latitude Electric field variability (ASHLEY). This model aims to improve specifications of soft electron precipitations and electric field variability that are not well represented in existing high-latitude empirical models. ASHLEY consists of three components, ASHLEY-A, ASHLEY-E and ASHLEY-Evar, which are developed based on the electron precipitation and bulk ion drift measurements from the Defense Meteorological Satellite Program (DMSP) satellites during the most recent solar cycle. On the one hand, unlike most existing high-latitude electron precipitation models, which have assumptions about the energy spectrum of incident electrons, the electron precipitation component of ASHLEY, ASHLEY-A, provides the differential energy fluxes in the 19 DMSP energy channels under different geophysical conditions without making any assumptions about the energy spectrum. It has been found that the relaxation of spectral assumptions significantly improves soft electron precipitation specifications with respect to a Maxwellian spectrum (up to several orders of magnitude). On the other hand, ASHLEY provides consistent mean electric field and electric field variability under different geophysical conditions by ASHLEY-E and ASHLEY-Evar components, respectively. This is different from most existing electric field models which only focus on the large-scale mean electric field and ignore the electric field variability. Furthermore, the consistency between the electric field and electron precipitation is better taken into account in ASHLEY.

1 **ASHLEY: A new empirical model for the high-latitude electron precipitation and electric**
2 **field**

3

4 **Qingyu Zhu¹, Yue Deng^{1*}, Astrid Maute², Liam Kilcommons³, Delores Knipp^{2,3}, Marc**
5 **Hairston⁴**

6

7 ¹Department of Physics, University of Texas at Arlington, Arlington, Texas, USA

8 ²High Altitude Observatory, National Center for Atmosphere Research, Boulder, Colorado, USA

9 ³Smead Aerospace Engineering Sciences, University of Colorado Boulder, Boulder, Colorado,

10 USA

11 ⁴William B. Hanson Center for Space Sciences, University of Texas at Dallas, Richardson,

12 Texas, USA

13

14 Corresponding author: Yue Deng (yuedeng@uta.edu)

15

16 **Key points:**

- 17 • ASHLEY better considers the consistency between the electric field and electron
18 precipitation than existing models.
- 19 • ASHLEY better incorporates IMF B_y polarity impacts on the electron precipitation and
20 improves soft electron precipitation specifications.
- 21 • ASHLEY provides consistent mean electric field and electric field variability.

22

23 **Abstract:**

24 In this study, a new high-latitude empirical model is introduced, named for Auroral energy
25 Spectrum and High-Latitude Electric field variability (ASHLEY). This model aims to improve
26 specifications of soft electron precipitations and electric field variability that are not well
27 represented in existing high-latitude empirical models. ASHLEY consists of three components,
28 ASHLEY-A, ASHLEY-E and ASHLEY-Evar, which are developed based on the electron
29 precipitation and bulk ion drift measurements from the Defense Meteorological Satellite
30 Program (DMSP) satellites during the most recent solar cycle. On the one hand, unlike most
31 existing high-latitude electron precipitation models, which have assumptions about the energy
32 spectrum of incident electrons, the electron precipitation component of ASHLEY, ASHLEY-A,
33 provides the differential energy fluxes in the 19 DMSP energy channels under different
34 geophysical conditions without making any assumptions about the energy spectrum. It has been
35 found that the relaxation of spectral assumptions significantly improves soft electron
36 precipitation specifications with respect to a Maxwellian spectrum (up to several orders of
37 magnitude). On the other hand, ASHLEY provides consistent mean electric field and electric
38 field variability under different geophysical conditions by ASHLEY-E and ASHLEY-Evar
39 components, respectively. This is different from most existing electric field models which only
40 focus on the large-scale mean electric field and ignore the electric field variability. Furthermore,
41 the consistency between the electric field and electron precipitation is better taken into account in
42 ASHLEY.

43

44 **1. Introduction**

45 Earth's ionosphere and thermosphere (I-T) system is closely coupled with the magnetosphere,
46 and the electromagnetic energy from magnetosphere is transferred into the I-T system through
47 field-aligned currents (FACs). The major part of electromagnetic energy is irreversibly converted
48 into heat through ohmic currents, and such heat is called Joule heating (Cole 1962; Thayer, 2000;
49 Richmond, 2020). Joule heating can significantly affect the I-T system both locally and globally
50 especially during geomagnetic storms. For example, the neutral temperature and density increase
51 due to the enhanced Joule heating during geomagnetic storms (e.g., Fuller-Rowell et al., 1994).
52 In addition, Joule heating can effectively change the global circulation within several hours,
53 which markedly alters the thermospheric compositions at different latitudes and can further
54 change the ionospheric electron density (e.g., Buonsanto, 1999; Prölss, 2011). Moreover, gravity
55 waves can be launched due to rapid variations of Joule heating and they can propagate globally,
56 causing large-scale traveling atmospheric disturbances and traveling ionospheric disturbances
57 (e.g., Lu et al., 2016, 2020). A comprehensive review of Joule heating and the I-T response to
58 Joule heating during geomagnetic storms can be found in Richmond (2020).

59 General circulation models (GCMs) of the I-T system are widely used to study variations of
60 the I-T system particularly during geomagnetic storms, and accurate estimations of Joule heating
61 are critical for reproducing observed features. Joule heating in GCMs is calculated from the
62 electric field, conductivities associated with the solar ionization and electron precipitation
63 together with the neutral winds (e.g., Lu et al., 1995). However, accurate estimations of Joule
64 heating is still challenging to date since it is difficult to capture the dynamic variations of the
65 electric field, ionospheric conductivity (mostly associated with the electron precipitation) and
66 neutral winds (e.g., Pedatella et al., 2018; Liemohn, 2020; Billet et al., 2018). In this paper, we

67 focus on the improvements of the electric field and electron precipitation in GCMs. Typically,
68 empirical models of electric field (e.g., Weimer, 2005; Heelis, 1982) and auroral electron
69 precipitation (e.g., Fuller-Rowell and Evans, 1987; Roble and Ridley, 1987; Newell et al., 2009)
70 are used to specify the high-latitude electric field and electron precipitation in GCMs,
71 respectively. Alternatively, high-latitude electric field and electron precipitation patterns derived
72 from data assimilation techniques, such as the Assimilative Mapping Ionospheric
73 Electrodynamics (AMIE) procedure (Richmond and Kamide, 1988; Richmond, 1992), can be
74 used. However, empirical models of electric field, electron precipitation and ionospheric
75 conductance are still needed in those assimilative techniques as background models. The
76 following deficiencies of the existing empirical models for high-latitude electrodynamic
77 forcings may contribute to the inaccurate Joule heating estimations:

78 1) Empirical models are good at capturing large-scale patterns under certain geophysical
79 conditions, but they may not well represent the electric field and electron precipitation patterns at
80 a specific time. In other words, the electric field and electron precipitation variabilities are not
81 well captured by empirical models. It has been shown that the magnitude of the electric field
82 variability is comparable with the magnitude of the large-scale mean electric field, so the electric
83 field variability can substantially contribute to Joule heating (e.g., Codrescu et al., 1995, 2000,
84 2008; Emery et al., 1999; Crowley & Hackert, 2001; Matsuo et al., 2003; Matsuo and Richmond,
85 2008; Cosgrove and Thayer, 2006; Fuller-Rowell et al., 2000; Rodger et al., 2001; Deng et al.,
86 2009; Fedrizzi et al., 2012). Therefore, an electric field variability model providing the variability
87 not captured by the large-scale mean electric field model may be needed to improve Joule
88 heating estimations in GCMs. Moreover, it is worth noting that the large-scale mean electric field
89 and electric field variability models need to be developed consistently, otherwise the actual

90 contribution of the electric field variability to Joule heating may not be well represented.
91 Furthermore, it is also worthwhile modeling the electric field and electron precipitation
92 variabilities consistently to improve Joule heating estimations in GCMs (e.g., Cosgrove and
93 Codrescu, 2009; Cosgrove et al., 2011; Zhu et al., 2018; Burleigh et al., 2019).

94 2) Even though the electric field and electron precipitation variabilities are captured, the I-T
95 system variations (especially in the F region) may still be imprecisely estimated. This may result
96 from inaccurate altitudinal ionospheric conductivity profiles so that the altitudinal Joule heating
97 distributions is incorrectly estimated in GCMs (Deng et al., 2008). It has been found that the
98 neutral density and temperature at F region altitudes are more sensitive to the Joule heating
99 deposited in the F-region than that deposited in lower altitudes (e.g., Deng et al., 2011; Huang et
100 al., 2012) especially on a short time scale (<0.5-1 day). The F-region conductivity and Joule
101 heating can be significantly underestimated owing to the underestimation of soft (<1 keV)
102 electron precipitations which are important ionization sources of the thermosphere at the F-
103 region altitudes (Rees, 1989). However, most existing auroral electron precipitation models
104 typically only provide the total energy flux together with the average energy (or total number
105 flux) and assume that the energy spectrum of incident electrons has a certain shape (e.g., Fuller-
106 Rowell and Evans, 1987; Y. Zhang and Paxton, 2008; Newell et al., 2009), which could lead to
107 inaccurate estimations of soft electron precipitations. For example, a Maxwellian spectrum is
108 typically assumed because the estimated ionospheric conductance based on such assumption
109 compares well with that calculated using measured ionospheric and thermospheric parameters
110 (e.g., Vickrey et al., 1981; Robinson et al., 1987). Nevertheless, it was found that a Maxwellian
111 spectrum may significantly underestimate the soft electron precipitation when comparing with
112 the energy spectrum from measurements, sometimes by orders of magnitude (e.g., McIntosh and

113 P. Anderson, 2014; Wing et al., 2019). Although additional types of energy spectra different
114 from a Maxwellian spectrum have been included in recently developed electron precipitation
115 models (e.g., Newell et al., 2009, 2014; B. Zhang et al. 2015), soft electron precipitations may
116 still be underestimated owing to deficient precipitation spectral identification techniques (Wing
117 et al., 2019) and incomplete inclusion of soft electron precipitations from different sources
118 (Khazanov and Glocer, 2020). Therefore, to better specify the altitudinal distribution of Joule
119 heating in GCMs and improve the GCM accuracy, it is critical to develop a new electron
120 precipitation model that can better specify the soft electron precipitations.

121 In this paper, a new empirical model aimed at improving the specifications of Auroral energy
122 Spectrum and High-Latitude Electric field variability, ASHLEY, is introduced. ASHLEY is
123 developed based on the electron precipitation and bulk ion drift measurements from the Defense
124 Meteorological Satellite Program (DMSP) satellites. ASHLEY consists of three components: 1)
125 an auroral electron precipitation component, ASHLEY-A, that provides the differential energy
126 fluxes of incident electrons in the 19 DMSP energy channels without making any assumptions
127 about the energy spectrum; 2) a high-latitude electric potential component, ASHLEY-E, that
128 specifies the large-scale mean electric field; 3) an electric field variability component, ASHLEY-
129 Evar, that quantifies the electric field variability not captured by ASHLEY-E. The remaining part
130 of this paper is organized as follows: Section 2 provides an overview of the datasets used for the
131 ASHLEY development and data processing procedures. The methodology used for the
132 development of ASHLEY is illustrated in Section 3. Section 4 provides statistical comparisons of
133 model to data, and Section 5 presents the outputs of ASHLEY. Section 6 discusses similarities
134 and differences between ASHLEY and models developed in previous studies along with the
135 directions for future improvements. The main conclusions are summarized in Section 7. More

136 details about fitting procedures and model reconstructions discussed in Section 3 are given in the
137 Appendix.

138

139 **2. Data preparation**

140 **2.1 DMSP measurements**

141 **2.1.1 Electron precipitation**

142 The in-situ auroral electron precipitation measurements from the DMSP F16-F18 satellites
143 during 2010-2015 are used in this study. All three satellites flew in circular Sun-synchronous
144 orbits at an altitude of ~ 840 km with an inclination of $\sim 98.8^\circ$. The measurements were taken by
145 the onboard Special Sensor for Precipitating Particles, version 5 (SSJ/5), which measures
146 incident electrons and ions from 30 eV and 30 keV every second using 19 logarithmically-spaced
147 energy channels (Hardy et al., 2008; Redmon et al., 2017). The field of view of the SSJ/5 is a 4°
148 by 90° fan ranging from the zenith to the horizon and the 90° field of view is divided into six 15°
149 zones. In this study, we will focus on the electron precipitation and particularly the differential
150 energy fluxes in 19 energy channels. The differential energy flux data are acquired from the
151 dataset created by Redmon et al. (2017) and details about the dataset can be found in that paper.
152 Overall, there are $>10^5$ polar crossings ($|\text{MLAT}| > 45^\circ$ segments of trajectories; MLAT=magnetic
153 latitude) with good data quality used in this study, and the number of polar crossings from the
154 Northern Hemisphere (NH) and Southern Hemisphere (SH) are roughly comparable (NH: 53348;
155 SH: 52670).

156 **2.1.2 Bulk Ion drift**

157 The Special Sensor for Ions, Electrons and Scintillation (SSIIES) onboard the DMSP satellite
158 measures the full bulk ion drift vector (\mathbf{V}) in the spacecraft coordinate system (i.e., $\mathbf{V} =$

159 $V_x \hat{x} + V_y \hat{y} + V_z \hat{z}$, where \hat{x} is along the satellite trajectory, \hat{z} is outward of the center of the
160 Earth and \hat{y} completes righthanded system; V_x , V_y and V_z are the components in directions
161 corresponding to their subscripts, respectively). In this study, bulk ion drift measurements from
162 the DMSP F15-F18 satellites during 2010-2018 are used. DMSP F16-F18 carry the latest version
163 of the SSIES (version 3) with a 1-s temporal resolution, whereas the DMSP F15 carries the
164 previous version of the SSIES (version 2) with a 4-s temporal resolution. Despite using different
165 versions of the SSIES, it is found that there are no significant deviations in the statistical electric
166 potential and electric field results in regions where all satellite flew by (not shown). In addition,
167 since the DMSP F15 data improve the data coverage at noon and midnight, DMSP F15 bulk ion
168 drift measurements are included in the dataset.

169 After removing the spacecraft velocity with respect to an Earth-centered corotating reference
170 frame, the residual ion drift vector has been used for the derivation of the electric potential and
171 electric field. Because the SSIES is sensitive to the background O^+ density concentration, the
172 measurements are generally in poor quality when the ionospheric O^+ density is low or other ion
173 species (such as H^+) are dominant. In this study, only data measured when the background O^+
174 concentration and density are relatively high (concentration: $>90\%$; density: $>4 \times 10^3 \text{ cm}^{-3}$) and
175 with the best quality flag (flag = 1) are used. If a polar crossing has many unavailable data (i.e.,
176 large data gap) or significant baseline issue, that polar crossing will be excluded in the final
177 dataset. Overall, more than half of the polar crossings in the original dataset are discarded
178 particularly in the local winter. The remaining dataset has more polar crossings from the northern
179 hemisphere than the southern hemisphere (NH: 51126; SH: 29602).

180 To calculate the electric field and electric potential, linear baseline corrections of V_x , V_y and
181 V_z components are applied to ensure they are zero at both ends of each polar crossing (i.e.,

182 $|\text{MLAT}|=45^\circ$ in this study). Since the V_x component is generally noisier than other components,
 183 the standard deviations of the V_x data measured in the first and last minute of each polar crossing
 184 are calculated prior to the baseline correction to ensure the reliability of the baseline. If both
 185 standard deviations are smaller than 100 m/s, the V_x data are baseline corrected and included in
 186 the dataset. Otherwise, the V_x data along that polar crossing are discarded and the electric field
 187 vector along that track is not calculated. In addition, only the large-scale V_x data (smoothed by a
 188 70-s sliding window) are utilized to avoid introducing unreliable small-scale and mesoscale
 189 structures in the V_x data. If all components of the bulk ion drift vector after the baseline
 190 correction (\mathbf{V}') are available, the electric field vector (\mathbf{E}) is calculated through $\mathbf{E} = -\mathbf{V}' \times \mathbf{B}_0$.
 191 Here, \mathbf{B}_0 is the background geomagnetic main field vector at the satellite location from the
 192 International Geomagnetic Reference Field-12 (IGRF-12) model (Thébault et al., 2015). The
 193 electric field vector is then decomposed into the magnetic eastward (E_{d1}) and equatorward (E_{d2})
 194 components as defined in the modified apex coordinate system using a reference height of 110
 195 km (Richmond, 1995). More details associated with the modified apex coordinates and the
 196 decomposition procedure can be found in Richmond (1995) and Laundal and Richmond (2017).
 197 The electric potential is calculated following a similar procedure used in Zhu et al. (2020a):
 198 The first step is to calculate the along-track electric field \mathbf{E}_x ($\mathbf{E}_x = E_x \hat{\mathbf{x}}$), which can be
 199 approximated through $E_x \approx -V_y' B_{0z}$. Here, V_y' is the horizontal cross-track ion drift vector after
 200 applying the baseline correction and B_{0z} is the vertical component of the \mathbf{B}_0 at the satellite
 201 location. The contribution of the vertical ion drift to E_x is generally small and is therefore
 202 neglected in our calculation. The next step is to integrate the along-track electric field to
 203 determine the electric potential along that pass. The subsequent step is to correct the calculated

204 electric potential to ensure its values are zero at both ends of each polar crossing. Details of the
 205 electric potential calculation can be found in Zhu et al. (2020a).

206 **2.2 IMF and solar wind data**

207 In this study, the interplanetary magnetic field (IMF) y and z (B_y and B_z) components in the
 208 Geocentric-Solar-Magnetospheric (GSM) coordinates are used (Note that the subscripts y and z
 209 have different meanings than those in the previous subsection). Two parameters are further
 210 calculated in this study: 1) the IMF transverse component magnitude, B_T , which represents the
 211 strength of the IMF projection onto the GSM Y-Z plane, i.e., $B_T = \sqrt{B_y^2 + B_z^2}$; 2) IMF clock
 212 angle (θ_c), which stands for the angle between GSM north and the IMF projection onto the GSM
 213 Y-Z plane and is given by $\theta_c = \text{atan2}(B_y, B_z)$. Note that a mirror correction (i.e., $\theta'_c = 360^\circ -$
 214 θ_c) has been applied for SH polar crossings in order to take the different impacts of the IMF B_y
 215 polarity on the high-latitude electrodynamic forcings in different hemispheres into account. In
 216 addition, the solar wind flow speed (V_{sw}) and solar wind proton density (N_{sw}) are used. The
 217 IMF and solar wind data used in this study are 5-min averaged data from the NASA/GSFC's
 218 OMNI data set through OMNIWeb. Similar to Zhu et al. (2020a), a 30-min propagation time
 219 delay is applied to account for the traveling time from the bow shock to the ionosphere.

220 **2.3 DMSP data categorization**

221 Each DMSP polar crossing is categorized according to two parameters, ε_t and θ_c , where:

$$222 \quad \varepsilon_t = V_{sw}^{4/3} B_T^{2/3} N_{sw}^{1/6} \quad (1)$$

222 ε_t (in the unit of $(\text{km})^{4/3} (\text{s})^{-4/3} (\text{nT})^{2/3} (\text{cm})^{-1/2}$) is essentially the combination of B_T and V_{sw}
 223 terms in the Newell coupling function (Newell et al., 2007) multiplied by $N_{sw}^{1/6}$. As discussed in
 224 Newell et al. (2007), the term $N_{sw}^{1/6}$ appeared in their derivation of the coupling function, but was

225 omitted on purpose to achieve better correlations with other parameters tested in their study.
226 However, they found that including the term $N_{SW}^{1/6}$ can slightly improve the correlation with the
227 auroral power. Meanwhile, Newell and Meng (1994) suggested that the soft electron
228 precipitation may depend on N_{SW} , so that the term $N_{SW}^{1/6}$ was kept in the expression of ε_t since
229 the soft electron precipitation is one major focus of this study. Moreover, the $\sin^{\frac{8}{3}}(\frac{\theta_c}{2})$ term
230 originally in the Newell coupling function is omitted in the expression of ε_t since the $\sin^{\frac{8}{3}}(\frac{\theta_c}{2})$
231 term cannot well distinguish positive and negative IMF B_y cases. Instead, Fourier fitting will be
232 performed to capture the IMF clock angle dependences of the electron precipitation, electric
233 potential and electric field variability.

234 The averaged ε_t and θ_c of a DMSP polar crossing are used to represent the IMF and solar
235 wind conditions corresponding to that polar crossing (the typical averaging period is about 20
236 minutes). If the IMF or solar wind data are missing, the corresponding polar crossing is
237 excluded. Moreover, polar crossings for which the standard deviation of ε_t is greater than 15% of
238 the average of ε_t of that polar crossing or the standard deviation of θ_c is greater than 22.5° are
239 also excluded. This procedure removes polar crossings during which the IMF or solar wind data
240 have large variations. We found about 30% polar crossings are excluded due to missing or
241 unsteady IMF/solar wind IMF data. Distributions of the IMF and solar wind data used for
242 ASHLEY-A and ASHLEY-E/ASHLEY-Evar developments are shown in Figures S1 and S2,
243 respectively.

244 For polar crossings with good electron precipitation data, all polar crossings for which ε_t is
245 smaller than 3,000 (roughly corresponds to the IMF $B_T < 1$ nT case under normal solar wind
246 conditions) are sorted into one category regardless of θ_c . Other polar crossings for which

247 $3,000 < \varepsilon_t < 30,000$ are sorted into 8 ε_t bins and 8 θ_c bins (i.e., $8 \times 8 + 1 = 65$ categories in total).
248 The 360° span of θ_c is evenly divided into 8 bins with each centered at a multiple of 45° . An
249 upper boundary of 30,000 (roughly corresponds to the IMF $B_T = 22$ nT case under normal solar
250 wind conditions) is set for ε_t to exclude a small amount of polar crossings ($\sim 1\%$) under very
251 strong IMF and solar wind conditions.

252 Likewise, for polar crossings with good electric field/potential data, all polar crossings for
253 which ε_t is smaller than 3000 are categorized as one category regardless of θ_c , and other polar
254 crossings with $3,000 < \varepsilon_t < 24,000$ (roughly corresponds to the IMF $B_T = 17$ nT case under normal
255 solar wind conditions) are sorted into 6 ε_t bins and 8 θ_c bins (i.e., $6 \times 8 + 1 = 49$ categories in total).
256 Fewer ε_t bins and smaller upper boundary of ε_t than those set to sort the electron precipitation
257 data are primarily due to the smaller amount of polar crossings with good electric field/potential
258 data. Tables 1a and 1b summarizes the lower and upper boundaries along with the median values
259 of different ε_t bins used to sort the electron precipitation and electric field/potential data,
260 respectively. Note that polar crossings from both hemispheres are combined together to achieve
261 best magnetic local time (MLT) coverage since the MLT coverage is limited in a single
262 hemisphere. In addition, polar crossings from all seasons are combined in this study to have good
263 data coverage for the distinct parameter bins in order to achieve statistically meaningful results.
264 In the future, the seasonal dependence will be added in the models if more data become
265 available.

266

267 **3. Model development**

268 **3.1 Fitting**

269 **3.1.1 Electron precipitation data**

270 For each ε_t - θ_c category, the differential energy flux (J_E) in each energy channel (19 energy
 271 channels in total) and above 50° MLAT are binned according to their MLTs and magnetic
 272 latitudes (MLATs). The sizes of the MLT and MLAT bins are 1 hour and 1° , respectively. If a
 273 bin has more than 100 data points, the average of the differential energy flux is calculated.
 274 Otherwise, the linear interpolation value based on the averages of the closest two MLT bins is
 275 used to deduce the average of that bin. The distributions of the average differential energy flux
 276 pattern are further smoothed in MLT and MLAT directions afterwards by using moving average
 277 smoothing.

278 With the smoothed average differential energy flux pattern in each energy channel, the next
 279 steps are to capture the MLT and IMF clock angle dependences of the differential energy flux in
 280 each latitudinal bin by using Fourier fitting. First, the differential energy flux in each bin of
 281 MLAT, ε_t , and θ_c is fitted to a Fourier series constructed by ϕ ($\phi = \frac{\text{MLT}}{12}\pi$). After the MLT
 282 fitting, the MLT Fourier coefficients from eight θ_c bins in each bin of MLAT and ε_t (except for
 283 the lowest ε_t bin) are then fitted to a Fourier series constructed by ω ($\omega = \frac{\theta_c}{180^\circ}\pi$) to capture the
 284 IMF clock angle variation. The MLT and IMF clock angle fittings are detailed in Appendix A1.

285 **3.1.2 Electric potential and electric field data**

286 The electrostatic potential (Φ) can be expanded in terms of spherical harmonics in a spherical
 287 coordinate system (Jackson, 2007). Following the approach shown in Weimer (1995), if only
 288 working with the real part of the spherical harmonics, Φ can be expressed as:

$$\Phi(\theta, \phi) = \sum_{l=0}^{12} F_{l0} P_l^0(\cos \theta) + \sum_{l=1}^{12} \sum_{m=1}^{\min(l,4)} (F_{lm} \cos m\phi + G_{lm} \sin m\phi) P_l^m(\cos \theta). \quad (2)$$

289 Here, P_l^m is the associated Legendre function, θ is the polar angle converted from the MLAT
 290 ($\theta = \frac{\pi - \lambda_m}{\pi} \pi$, where λ_m is the MLAT in radians) and ϕ is the azimuthal angle which is the same
 291 as that defined in Section 3.1.1. The expansion is terminated at $l=12$ and $m=4$ to avoid unrealistic
 292 small-scale and mesoscale structures associated with higher order terms.

293 In addition to the electric potential data, the electric field (E_{d1} and E_{d2}) data are also used in
 294 the fitting procedure to provide more constraints on the electric potential fitting. The
 295 relationships between Φ and E_{d1} and between Φ and E_{d2} can be found in Eqs. 4.8 and 4.9 in
 296 Richmond (1995), respectively. Details about the expansion of E_{d1} and E_{d2} in terms of the
 297 spherical harmonics can be found in Appendix A2. With all Φ , E_{d1} and E_{d2} data along with their
 298 locations in each $\varepsilon_t - \theta_c$ category, F_{lm} and G_{lm} can be obtained from a least-square fit. Details of
 299 the fitting procedure can be found in Appendix A2. Then F_{lm} and G_{lm} from eight θ_c bins in each
 300 ε_t bin (except the lowest ε_t bin) are fitted to a Fourier series constructed by ω to capture their
 301 IMF clock angle variations using the same procedures described in Section 3.1.1.

302 **3.1.3 Residual electric field data**

303 Once the ASHLEY-E component has been developed, the difference between the measured
 304 and modeled electric field along a polar crossing can be calculated. Each component of the
 305 residual electric field E'_{di} ($i=1, 2$) above 50° MLAT are binned according to its MLT and MLAT
 306 for each $\varepsilon_t - \theta_c$ category. The sizes of the MLT and MLAT bins are 1 hour and 2° , respectively.
 307 Larger MLAT bin size than that used for the electron precipitation data binning is due to smaller
 308 amount of electric field data. The standard deviations of E'_{d1} and E'_{d2} , namely σ_1 and σ_2 , in each
 309 bin (if has >100 data points) are calculated and are used to quantify the magnitudes of E_{d1} and
 310 E_{d2} variabilities.

311 After obtaining the preliminary MLAT-MLT distributions of σ_1 and σ_2 for each ε_t -
312 θ_c category, the next step is to fill the data gaps in each MLAT bin by using the linear
313 interpolation results based on the values in the adjacent two MLT bins. Then, the distributions of
314 σ_1 and σ_2 are smoothed in both MLT and MLAT directions by using the sliding window
315 smoothing. After that, σ_1 and σ_2 in each bin of MLAT, ε_t and θ_c are fitted to a Fourier series
316 constructed by MLT to capture their MLT variations. Then, the MLT Fourier coefficients from
317 eight θ_c bins in each bin of MLAT and ε_t (except for the lowest ε_t bin) are fitted to a Fourier
318 series constructed by the IMF clock angle to capture the IMF clock angle variation. The MLT
319 and IMF clock angle fitting procedures are the same as those described in Section 3.1.1, and
320 details can be found in Appendix A1.

321 **3.2 Extrapolation and expansion**

322 With the fitting procedures described in Section 3.1, the electron precipitation pattern can be
323 reconstructed for any $\varepsilon_t \leq 22770$ and any θ_c , and the procedures are elaborated in Appendices
324 A3. Similarly, the electric potential and electric field variability patterns can be reconstructed for
325 any $\varepsilon_t \leq 18357$ and any θ_c , and the procedures are elaborated in Appendices A4. However,
326 since the range of ε_t covered by the dataset used in this study is limited, extrapolations and
327 expansions are performed for ASHLEY-A when ε_t exceeds 22770 and for ASHLEY-
328 E/ASHLEY-Evar when ε_t exceeds 18357. The detailed procedures are further described in this
329 subsection.

330 **3.2.1 Extrapolation**

331 **3.2.1.1 ASHLEY-A**

332 The extrapolation of ASHLEY-A is done by tracking the hemispheric-integrated differential
333 energy flux in different energy channels. The hemispheric-integrated differential energy flux is

334 defined as the integration of the down-going differential energy flux (πJ_E) over the polar
335 hemisphere ($|\text{MLAT}| > 45^\circ$) by assuming that the differential energy flux is pitch angle isotropic.
336 Figure 1 shows hemispheric-integrated differential energy fluxes in the 19 energy channels from
337 all 8 ε_t - θ_c bins (used for the development of AHSLEY-A) where θ_c is centered at 225° . As
338 shown in Figure 1, the hemispheric-integrated differential energy fluxes in the highest 11 energy
339 channels (central energy > 500 eV) increase approximately linearly with ε_t , while the
340 hemispheric-integrated differential energy flux tends to increase quadratically with ε_t in the
341 lowest 8 energy channels. Similar trends can also be found when θ_c has different values although
342 the increment rate varies with θ_c .

343 The trends shown in Figure 1 are used to extrapolate the hemispheric-integrated differential
344 energy in the highest 11 energy channels when $\varepsilon_t > 22,770$. In each energy channel, the
345 hemispheric-integrated differential energy flux at ε_t can be predicted according to the best-fit
346 line at the given θ_c . The slope and y-intercept of the best-fit line at θ_c can be determined using
347 the Fourier fitting results of the slopes and y-intercepts from the 8 θ_c bins, respectively. The ratio
348 between the predicted hemispheric-integrated differential energy flux by the best-fit line and the
349 hemispheric-integrated differential energy flux from the modeled pattern at θ_c and $\varepsilon_t = 22,770$ in
350 each channel is calculated as the scaling factor. The extrapolated differential energy flux pattern
351 at θ_c and ε_t is the modeled differential energy flux pattern at θ_c and $\varepsilon_t = 22,770$ multiplied by the
352 scaling factor.

353 For the lowest 8 energy channels, it is assumed that the increase of the hemispheric-integrated
354 differential energy flux for $\varepsilon_t > 22,770$ follows the same increase rate between $\varepsilon_t = 17,590$ and
355 $\varepsilon_t = 22,770$ in each channel at the given θ_c . Although such method may underestimate
356 contributions from < 500 eV electron precipitations for a very large ε_t than a quadratic

357 extrapolation, this method can at least provide a lower limit for <500 eV electron precipitations
 358 at a very large ε_t since the available data are limited when ε_t is very large. Again, the ratio
 359 between the predicted hemispheric-integrated differential energy flux and the hemispheric-
 360 integrated differential energy flux from the modeled pattern at θ_c and $\varepsilon_t=22,770$ in an energy
 361 channel is calculated as the scaling factor, which is further multiplied to the modeled differential
 362 energy flux pattern at θ_c and $\varepsilon_t=22,770$ to obtain the extrapolated differential energy flux pattern
 363 for that energy channel.

364 **3.2.1.2 ASHLEY-E and ASHLEY-Evar**

365 Since the electric field variability is supposed to be consistent with the background electric
 366 field model, the same extrapolation procedures are used for ASHLEY-E and ASHLEY-Evar,
 367 which are based on the extrapolation of the cross-polar-cap potential (CPCP) described in the
 368 following paragraph.

369 Figure 2 shows the CPCP outputs of ASHLEY-E from all 6 ε_t - θ_c bins (used for the
 370 development of ASHLEY-E and ASHLEY-Evar) where θ_c is centered at 180° . As expected, the
 371 CPCP increases with ε_t . However, it was found that the CPCP may be saturated at a certain point
 372 under intense solar wind and IMF conditions (e.g., Shepherd, 2007 and references therein).

373 Therefore, to account for the saturation of the CPCP at a large ε_t , the CPCP (Φ_{PC}) is assumed to
 374 be linear with β , where

$$\beta = \frac{\varepsilon_t}{\sqrt{1 + \left(\frac{\varepsilon_t}{\varepsilon_{inf}}\right)^2}} \quad (3)$$

375 ε_{inf} is an adjustable parameter which is set to be 40,000 to fit the trend shown in Figure 2 so

376 that Φ_{PC} saturates at the level of ~ 190 kV comparable to the level reported in Hairston et al.

377 (2005). The procedure is repeated for other IMF clock angles by using $\varepsilon_{inf} = 40,000$. It is found

378 that the Φ_{PC} from ASHLEY-E is ~ 90 kV under the extreme IMF and solar wind conditions
379 reported in Mitchell et al. (2010), which is comparable to the values reported in their study (80-
380 100 kV). Similarly, the reversal convection potential (the potential across the reversal cells) from
381 ASHLEY-E is about ~ 19 kV under the extreme IMF and solar wind conditions reported in
382 Wilder et al. (2008), which is also comparable to the values reported in their study (15-20 kV).
383 Therefore, our method and the choice of ε_{inf} can well capture the electric potential saturation in
384 general. To obtain the CPCP at a given $\varepsilon_t > 18357$ and a given θ_c , the CPCP can be predicted
385 according to the best-fit curve. The ratio of the predicted CPCP and the CPCP at $\varepsilon_t = 18357$ and
386 θ_c is calculated as the scaling factor, which is then used to scale the electric potential and electric
387 field variability patterns constructed at $\varepsilon_t = 18357$ and θ_c ,

388 **3.2.2 Expansion**

389 The electron precipitation and electric potential (electric field) patterns expand as the solar
390 wind and IMF conditions become more intense (e.g., Feldstein and Starkov, 1967; Weimer,
391 2005), which is also considered in ASHLEY. In this study, expansions of the poleward auroral
392 boundary (PAB) and convection reversal boundary (CRB) on the dawn (4-8 MLT) and dusk (16-
393 20 MLT) sides are used to quantify the expansions of electron precipitation and electric field
394 patterns, respectively.

395 Figure 3a shows the averaged co-MLAT (r) of the PAB determined on the dawn and dusk
396 sides along the same polar crossing by using the technique developed by Kilcommons et al.
397 (2017) from as a function of ε_t when $157.5^\circ < \theta_c < 202.5^\circ$. Similarly, Figure 3b shows the
398 averaged co-MLAT of the CRB determined on the dawn and dusk sides by using the technique
399 developed by Zhu et al. (2020a) as a function of ε_t when $157.5^\circ < \theta_c < 202.5^\circ$. The CRB is found
400 to be a good indicator of the polar cap boundary especially under southward IMF conditions

401 (e.g., Sotirelis et al., 2005), and the polar cap boundary was found to saturate at around $r=21^\circ$
402 under southward IMF conditions (e.g., Ridley et al., 2004; Merkin et al., 2007). To take the
403 saturation of the polar cap area into account, the co-MLAT of the CRB is assume to be linear
404 with β defined in Eq. 3. The adjustable ε_{inf} is set to be 22,000 so that the best-fit curve
405 according to the black dots shown in Figure 3b saturates at around $r =21^\circ$. A similar approach is
406 applied to capture the expansion of the PAB, and since the polar cap boundary is found to be
407 slightly poleward of the poleward of the PAB in general (Newell et al., 2004), so it is assumed
408 that the PAB saturates slightly equatorward of the CRB. The adjustable ε_{inf} is set to be 17,000
409 so that the best-fit curve according to the black dots shown in Figure 3a saturates at around r
410 $=23^\circ$ and the offset between the fitted CRB and PAB is roughly constant (2°) when $\varepsilon_t > 20000$.
411 The choice of ε_{inf} for the PAB can be improved in the future based on a comprehensive study of
412 the locations of the PAB and CRB under intense southward IMF conditions.

413 The expansions of the PAB and CRB in other θ_c bins are captured in a similar approach using
414 the same ε_{inf} values determined in the $157.5^\circ < \theta_c < 202.5^\circ$ bin, except for the CRB in θ_c bins
415 which are centered at 315° , 0° and 45° since the CRB is typically difficult to be identified from
416 the observation under IMF B_z northward and dominant conditions. The IMF clock angle
417 dependences of the slope and y-intercept of the best-fit r - β line are then determined by a Fourier
418 expansion with respect to the IMF clock angle.

419 The expansion rate of the PAB can be determined by the ratio of the values of r on the best-fit
420 r - β line of the PAB at the given ε_t and $\varepsilon_t = 22,770$ and at the given θ_c . Once the expansion rate
421 of the PAB is determined, the extrapolated differential energy flux pattern is radially expanded
422 according to the expansion rate. However, it is worth noting that the differential energy flux
423 needs to be scaled down by the square of the expansion rate of the PAB in order to maintain the

424 same hemispheric-integrated differential energy flux. Likewise, the expansion rate of the CRB
425 can be determined by the ratio of the values of r on the best-fit r - β line of the CRB at the given
426 ε_t and $\varepsilon_t = 18,357$ and at the given θ_c between 90° and 270° . For the expansion rate of the CRB
427 for $\theta_c < 90$, it is assumed that the expansion rate is 1 (i.e., no expansion) at $\theta_c = 0^\circ$ and is a
428 linear function of $\sin^2(\frac{\omega}{2})$ between $\theta_c = 0^\circ$ and $\theta_c = 90^\circ$ ($\omega = \frac{\theta_c}{180^\circ} \pi$). Similarly, for the
429 expansion rate of the CRB for $\theta_c > 270^\circ$, it is assumed that the expansion rate is 1 at $\theta_c = 360^\circ$
430 and is a linear function of $\sin^2(\frac{\omega}{2})$ between $\theta_c = 270^\circ$ and $\theta_c = 360^\circ$. Once the expansion rate
431 of the CRB is determined, the extrapolated electric potential and electric field variability patterns
432 are radially expanded according to the expansion rate. However, the modeled electric field
433 variability needs to be downscaled by the expansion rate of the CRB to ensure that the ratio
434 between the electric field variability and the background mean electric field does not change as
435 the electric potential pattern expands radially.

436

437 **4. Statistical comparisons of model to data**

438 The modeled results along each polar crossing used in the ASHLEY development are
439 calculated under its corresponding ε_t and θ_c , and the modeled and measured data in each ε_t - θ_c
440 bin are binned according to their MLATs and MLTs. Comparisons between the binning results
441 of the modeled and measured data from some specific ε_t - θ_c bins can be found in supplement
442 Figures S3-S5. Here we focus on comparisons from all ε_t - θ_c bins used for the ASHLEY
443 development.

444 Figure 4 compares averages of the modeled and measured differential energy flux data from
445 all MLAT-MLT and ε_t - θ_c bins used for the ASHLEY-A development. The sizes of MLAT and
446 MLT bins are 1° and 1 h, respectively, so that the numbers of the MLT, MLAT and ε_t - θ_c bin are

447 24, 40 (50°-90° MLAT) and 65, respectively. Likewise, Figures 5a-5c compare averages of the
448 modeled and measured electric potential, E_{d1} and E_{d2} from all MLAT-MLT and ε_t - θ_c bins used
449 for the ASHLEY-E development, respectively. Figures 5d and 5e serve as validations of
450 ASHLEY-Evar. In each plot, the x-axis value of a grey dot represents the standard deviations of
451 measured E_{di} ($i=1,2$) in a MLAT-MLT bin of an ε_t - θ_c bin used for the ASHLEY-Evar
452 development, and the y-axis value of a grey dot denotes the root mean squares of modeled σ_i
453 ($i=1,2$) in the same MLAT-MLT bin. For Figure 5, the MLAT bin size is 2° and the MLT bin
454 size is 1 h, so that the numbers of the MLT, MLAT and ε_t - θ_c bins are 24, 20 (50°-90° MLAT)
455 and 49, respectively.

456 Overall, all the grey dots are concentrated around the $y=x$ line (blue-dashed line) and the best-
457 fit line (red-thick line) according to the grey dots does not significantly deviate from the $y=x$
458 line. Figures 4 and 5 along with Figures S3-S5 manifest that all components of the ASHLEY
459 model generally work well in a statistical sense.

460

461 **5. Model outputs**

462 **5.1 ASHLEY-A outputs**

463 Figure 6 shows the ASHLEY-A outputs of the differential energy flux in the 19 DMSP energy
464 channels when the IMF is purely southward (IMF $B_z=-8$ nT, $V_{sw}=450$ km/s and $N_{sw}=4$ cm⁻³).
465 Figure 6 indicates that >500 eV electrons mainly precipitate on the night side while <500 eV
466 electrons are more likely to precipitate on the day side and are located at higher MLATs
467 than >500 eV electron precipitations. Meanwhile, a salient peak can be found near the magnetic
468 noon and between 70° and 75° MLAT in channels of which the central energy is around 100 eV.
469 The peak location may correspond to the dayside cusp location since the electrons precipitating

470 into the cusp are typically found to have the average energy around 100 eV (Newell and Meng,
471 1988).

472 Figure 7 compares the modeled differential energy fluxes in three DMSP energy channels
473 when the IMF is purely northward, eastward, westward and southward (IMF $B_T=-8$ nT, $V_{SW}=450$
474 km/s and $N_{SW}=4$ cm⁻³). For >1 keV electrons, the precipitation is most intense and equatorward
475 for the southward IMF case. By contrast, the precipitation is weakest and occurs most poleward
476 for the northward IMF case. Moreover, the electron precipitation does not differ significantly
477 under positive and negative IMF B_y conditions. However, unlike >1 keV electron precipitations,
478 the magnitude of the dayside peak shown in the ~100 eV channel is weakest under purely
479 southward IMF conditions and is strongest under purely northward IMF conditions. In addition,
480 the location of the dayside peak appears to depend on the IMF B_y polarity. The peak location
481 tends to shift to the dawn side as the IMF B_y becomes more negative, indicating that the cusp
482 shifts to the dawn side as the IMF B_y becomes more negative, which is consistent with previous
483 findings (e.g., Candidi et al., 1983; Newell et al., 1989).

484 Figure 8a serves as an example to illustrate how the modeled energy spectrum deviates from a
485 Maxwellian spectrum determined from the total energy flux (Q_0) and average energy (\bar{E}) of the
486 modeled spectrum. The average energy can be calculated from the modeled spectrum by using
487 the Eq. 2 in Robinson et al. (1987), and the lower and upper boundaries of the integral in the
488 numerator and denominator of that equation are 500 eV and 30 keV, respectively. The total
489 energy flux is calculated by multiplying a factor of π to the numerator of that equation by
490 assuming the downward differential energy flux is isotropic. The IMF and solar wind conditions
491 for the case shown in Figure 8a are: the IMF $B_y=0$, the IMF $B_z=-8$ nT, $V_{SW}=450$ km/s and
492 $N_{SW}=4$ cm⁻³, and the location is on the dawn side (MLT =4.5 h, MLAT=64.5°). For the modeled

493 spectrum (red dots) shown in Figure 8a, $Q_0 = 4.87 \text{ mW/m}^2$ and $\bar{E} = 5.08 \text{ keV}$, and the derived
 494 Maxwellian spectrum is indicated by blue crosses. As compared with the modeled spectrum (red
 495 dots), the Maxwellian spectrum overestimates 1-10 keV electrons and underestimates both <1
 496 keV and >10 keV electrons. More importantly, the Maxwellian spectrum markedly
 497 underestimates <1 keV electron precipitations. In particular, the difference is approximately 2
 498 orders of magnitude for ~ 100 eV electrons. Hence, the contribution of soft electron precipitations
 499 to the I-T system can be significantly underestimated if a Maxwellian energy spectrum is
 500 assumed.

501 **5.2 ASHLEY-E and ASHLEY-Evar outputs**

502 Figure 9 shows the electric potential outputs from ASHLEY-E for 8 different IMF clock
 503 angles, and other IMF and solar wind parameters for the cases shown in Figure 9 are: the IMF
 504 $B_T = 8 \text{ nT}$, $V_{SW} = 450 \text{ km/s}$ and $N_{SW} = 4 \text{ cm}^{-3}$. In general, the electric potential displays a two-cell
 505 pattern except for the northward IMF B_z case, where a multiple-cell pattern appears. In addition,
 506 the negative cell on the dusk side and the positive cell on the dawn side are shaped into round
 507 and crescent cells, respectively, when the IMF B_y is positive. The opposite is true for the
 508 negative IMF B_y case. Meanwhile, the round cell typically has a larger absolute extremum than
 509 the crescent cell. Moreover, as shown in Figure 11a, the CPCP varies with the IMF clock angle,
 510 which maximizes and minimizes when the IMF B_z is purely southward and northward,
 511 respectively. Overall, the outputs from ASHLEY-E are consistent with previous studies (e.g.,
 512 Thomas and Shepherd, 2018 and references therein).

513 Figure 10 compares the mean electric field magnitude ($E_1 = \sqrt{\bar{E}_{d1}^2 + \bar{E}_{d2}^2}$) and electric field
 514 variability magnitude ($E_2 = \sqrt{\sigma_1^2 + \sigma_2^2}$) for different IMF clock angles. For the cases shown in
 515 Figure 10, the conditions are: the IMF $B_T = 8 \text{ nT}$, $V_{SW} = 450 \text{ km/s}$ and $N_{SW} = 4 \text{ cm}^{-3}$. \bar{E}_{d1} and \bar{E}_{d2}

516 are calculated from the electric potential outputs of ASHLEY-E by using Eqs. 4.8 and 4.9 in
517 Richmond (1995), and σ_1 and σ_2 are direct outputs of ASHLEY-Evar. As shown in Figure 10a,
518 E_1 typically displays a three-peak structure and a more complex pattern appears when the IMF B_z
519 is purely northward. Figure 10b shows that E_2 tends to peak on the dawn and dusk sides when
520 the IMF is purely southward and the peak on the dawn side has a higher magnitude, while it
521 tends to have a single peak on the day side when the IMF is purely northward. In addition, the
522 distribution of E_2 depends on the IMF B_y polarity: E_2 tends to peak on the morning side when the
523 IMF B_y is positive with a relatively wider MLT span, whereas it tends to peak near noon when
524 the IMF B_y is negative with a weaker magnitude and a narrower MLT span. However, when the
525 IMF has a southward component, the MLT spans of the E_2 peak seems to be comparable for
526 positive and negative IMF B_y cases. Figure 11b further compares the IMF clock angle
527 dependences of the averaged E_1 and E_2 over the $|\text{MLAT}| > 60^\circ$ region. In general, both of the
528 averaged E_1 and E_2 maximize when the IMF is purely southward and the polar average of E_2 is
529 generally comparable with the polar average of E_1 when the IMF has a southward component.
530 However, the polar average of E_2 is much larger than the polar average of E_1 when the IMF is
531 northward. The results shown in Figures 10 and 11b are consistent with results shown in Matsuo
532 et al. (2003) in general.

533 **6. Discussion**

534 **6.1 Similarities and differences with previous empirical models**

535 The large-scale high-latitude electric field and electron precipitation have been studied for
536 several decades and several empirical models have been established for the electric field (e.g.,
537 Papitashvili and Rich, 2002; Weimer, 2005; Cousins and Shepherd, 2010) and electron
538 precipitations (e.g., Hardy et al., 1985, 1987; Fuller-Rowell and Evans, 1987; Y. Zhang and

539 Paxton, 2008; Newell et al., 2009, 2014) based on different measurements. However, to our
540 knowledge, existing electric field models and electron precipitation models have been developed
541 separately. As a consequence, the consistency between the electric field and electron
542 precipitation models is lacking. For example, Sheng et al. (2019) found that the CRB from the
543 Weimer (2005) convection model is significantly equatorward (up to $>10^\circ$ in MLAT) of the PAB
544 from the Fuller-Rowell and Evans (1987) electron precipitation model under intense southward
545 IMF and solar wind conditions, which may contradict the understanding established in previous
546 studies (e.g., Sotirelis et al., 2005). In addition, the simulations conducted in Sheng et al. (2019)
547 indicated that the large offsets between the CRB and PAB result in significant underestimations
548 of Joule heating. A primary advantage of ASHLEY is that the electron precipitation and electric
549 field components have been developed concurrently and, as much as possible, consistently. For
550 example, in addition to using electric field and electron precipitation data from the same platform
551 (DMSP satellite) and same solar cycle (solar cycle 24), the consistency between the CRB and
552 PAB has also been taken into account under intense IMF and solar wind conditions (see Section
553 3.2.2). Apart from improving the consistency between the electron precipitation and electric field
554 components, ASHLEY also improves specifications of the soft electron precipitation and electric
555 field variability.

556 **6.1.1 Soft electron precipitation**

557 Although several electron precipitation models have been developed (see Section 1), most of
558 them only provide the total energy flux, total number flux and average energy of an assumed
559 Maxwellian energy spectrum. Apart from those models, Hardy et al. (1985) established
560 distributions of the average spectrum in 7 Kp bins (Kp range: 0-6) based on 2.5 years of DMSP
561 SSJ3 measurements. Although the datasets used in this study and used in Hardy et al. (1985) are

562 from two different solar cycles and two different versions of SSJ, our results are qualitatively
563 consistent with Hardy et al. (1985). However, the K_p index is a low-resolution (3-h)
564 geomagnetic index, and the IMF and solar wind conditions can be considerably different even
565 though the K_p index is similar. Thus, the electron precipitation evolutions may not be well
566 captured in a K_p-based electron precipitation model. Therefore, a K_p-based electron
567 precipitation model may provide same electron precipitation patterns for 3 hours while an
568 electron precipitation model based on the IMF and solar wind may better capture the evolution of
569 the electron precipitation in such case. Moreover, a positive IMF B_y condition probably gives a
570 very similar K_p as a negative IMF B_y condition as long as the magnitude of B_y and solar wind
571 conditions are similar (Newell et al., 2008). However, as shown in Figure 8, the differences in
572 the soft electron precipitation are significant when the direction of the IMF B_y is opposite
573 although differences in the keV electrons are less significant. Therefore, the IMF B_y dependence
574 of the soft electron precipitation may not be well specified in the statistical patterns built by
575 Hardy et al. (1985) as compared with those provided by ASHLEY-A. Furthermore, ASHLEY-A
576 can provide distributions of the energy spectrum under intense IMF and solar wind conditions
577 based on reasonable extrapolations and expansions. Therefore, ASHLEY-A can be more useful
578 in studying the I-T system during intense geomagnetic storms when coupling into GCMs.

579 In addition to the Hardy model, the Ovation Prime (OP) models developed by Newell et al.
580 (2009, 2014) also improve the energy spectrum specification in empirical models. The major
581 characteristic of the OP models is that they provide the total energy flux, total number flux and
582 probability of three types of electron precipitations: diffuse, mono-energetic and broadband.
583 However, it is still challenging to correctly identify the precipitation type to date (e.g., Dombeck
584 et al., 2018; Wing et al., 2019). For example, as pointed out by Wing et al (2019), it is highly

585 possible that an energy spectrum matches none of the above three types and is labeled as the
586 diffuse type for simplicity and convenience, so that the diffuse precipitation may still dominate
587 in the OP models. Moreover, like the K_p index, the Newell coupling function used to drive OP
588 models does not distinguish the IMF B_y polarity either. Furthermore, the total energy flux, total
589 number flux and probability in each MLAT-MLT bin from the OP models is assumed to be
590 linear with the Newell coupling function. However, a linear fitting may underestimate the
591 evolution of <500 eV electron precipitations as implied by Figure 1. Therefore, the contribution
592 of the soft electron precipitation may still not be accurately estimated in the OP models.

593

594 **6.1.2 Electric field variability**

595 While most electric field models only provide large-scale high-latitude mean electric fields,
596 there are some efforts in studying the statistical distribution of the high-latitude electric field
597 variability. For example, Codrescu et al. (2000) established the electric field variability pattern in
598 10 auroral activity index bins and in different seasons according the Millstone Hill incoherent
599 scatter radar (ISR) measurements. Similarly, Cosgrove and Thayer (2006) established a K_p-
600 based statistic pattern based on Sondrestrom ISR measurements in a limited latitudinal region.
601 Matsuo et al. (2003) studied the distributions of the mean electric field and electric field
602 variability at high latitudes under several different IMF conditions and in different seasons based
603 on the Dynamic Explorer 2 (DE-2) satellite ion bulk drift measurements and the Weimer (2001)
604 empirical electric potential model which is also developed based on the DE-2 data. Moreover,
605 Matsuo and Richmond (2008) further analyzed the distribution of the electric field variability on
606 different scales under several different IMF conditions and in different seasons, and they found
607 that the large-scale electric field variability tends to be larger than the small-scale and mesoscale

608 electric field variabilities. Similar conclusion has been reached by Cosgrove et al. (2011) based
609 on Sondrestrom ISR measurements. Later, Cousins and Shepherd (2012) developed several
610 statistical maps of the small-scale and mesoscale electric field variabilities for different
611 interplanetary electric fields, in different seasons and in different hemispheres based on Super
612 Dual Auroral Radar Network (SuperDARN) radar measurements. Although statistical patterns of
613 high-latitude electric field variability have been established under different geophysical
614 conditions, a dynamic empirical electric field variability model that is consistent with the
615 background large-scale mean electric field model is still lacking to date. To our knowledge, the
616 empirical model used in Deng et al. (2009) is the only existing empirical model provide
617 consistent mean electric field and electric field variability which is based on the DE-2 ion bulk
618 drift measurements. The methodology used to develop that model is implemented in the
619 development of ASHLEY-E and ASHLEY-Evar. In comparison to the model used in Deng et al.
620 (2009), the solar wind dependences of the electric field and electric field variability are
621 implemented in ASHLEY-E and ASHLEY-Evar while the seasonal dependences of the electric
622 field and electric field variability are not taken into account. Meanwhile, the expansions of the
623 electric potential and electric field variability patterns are considered in ASHLEY-E and
624 ASHLEY-Evar under intense IMF and solar wind conditions.

625

626 **6.2 Low-energy tail of the energy spectrum**

627 The strong low-energy tail shown in the ASHLEY-A energy spectrum (Figure 8a) is
628 frequently seen in observations (e.g., Evans, 1974; Fung and Hoffman, 1988; Hardy et al., 1985;
629 McIntosh and Anderson, 2014; Wing et al., 2019) and its sources are considerably complex since
630 the electron precipitation is not a simple one-way transport of electrons from the magnetosphere

631 to the ionosphere (Khazanov and Glocer, 2020, and references therein). For example, if a field-
632 aligned potential drop is present, the upgoing electrons without sufficient kinetic energy to
633 overcome such potential drop will be reflected downward and subsequently are observed as
634 downward precipitation flux (Evans, 1994; Evans and Moore, 1979; Richards, 2013). In
635 addition, it is also possible that the upgoing superthermal electrons from the conjugate
636 hemisphere contribute to the formation of the low-energy tail (Khazanov and Glocer, 2020).

637 Meier et al. (1989) developed an empirical formula (hereafter, M89 formula) to account for
638 the low-energy tail which was later used in the model developed by Strickland et al. (1993). The
639 blue dashed line in Figure 8b shows the spectrum constructed by the M89 formula using $Q_0 =$
640 4.87 mW/m^2 , $\bar{E} = 5.08 \text{ keV}$ (hereafter, M89-I spectrum). Although the low-energy tail has been
641 significantly improved in contrast to a simple Maxwellian energy spectrum, the magnitude of the
642 low-energy tail is still underestimated by 50% in comparison with that of the ASHLEY energy
643 spectrum in general. However, it is worth noting that the M89 formula is based on the total
644 energy and average energy of the whole energy spectrum while the total energy and average
645 energy outputs of ASHLEY-A are calculated by using the $>500 \text{ eV}$ portion of the energy
646 spectrum (Section 5.1). The total energy and average energy calculated from the whole energy
647 spectrum shown in Figure 8a are $Q'_0 = 5.01 \text{ mW/m}^2$ and $\bar{E}' = 2.92 \text{ keV}$, respectively, and the
648 corresponding spectrum calculated from the M89 formula is indicated by the green dashed line in
649 Figure 8b (hereafter, M89-II spectrum). It is clear that the low-energy tail calculated by using
650 Q'_0 and \bar{E}' is more comparable with that of the ASHLEY-A energy spectrum as compared with
651 the low-energy tail calculated by using Q_0 and \bar{E} . However, the discrepancies of 1-10 keV
652 electrons between the M89-II and ASHLEY-A spectra are larger than those between the M89-I
653 and ASHLEY-A spectra. The discrepancy shown in Figure 8b is a general case in the auroral

654 oval although it may vary quantitatively with the location. Therefore, the ionospheric conductances
655 may be significantly overestimated in the auroral zone when the M89-II spectrum is utilized to
656 drive a GCM, and it might be necessary to propose a new empirical formula for the incident
657 electron energy spectrum in order to obtain the I-T responses at both E-region and F-region
658 altitudes correctly. In addition to the empirical formula, physical-based models such as the
659 SuperThermal Electron Transport (STET) model developed by Khazanov et al. (2014) may also
660 be useful to reconstruct the low-energy tail. It would be interesting to compare the performance
661 of different methods in representing the low-energy tail in the future.

662 The downward low-energy precipitation flux can lead to ionizations of the thermosphere at
663 the F-region altitudes, which increases the F-region conductivity but may not significantly
664 change the height-integrated conductivity (i.e., conductance). Therefore, the altitudinal Joule
665 heating distribution will be significantly changed, which may cause significant changes of the I-
666 T system. The impacts of soft electron precipitations on the I-T system will be more
667 comprehensively investigated in the future by coupling the ASHLEY model to a GCM. There
668 are also other mechanisms altering the altitudinal Joule heating, such as Alfvén waves incident
669 from the magnetosphere (e.g., Lotko and Zhang, 2018; Verkhoglyadova et al., 2018; Hogan et
670 al., 2020). The relative significance of two different mechanisms to the I-T system under
671 different conditions will also be an interesting topic that deserves future explorations.

672

673 **6.3 Future improvements**

674 As more data become available, we plan to incorporate seasonal variation in ASHLEY. For
675 example, it is found that the distribution and magnitude of the electron precipitation display
676 seasonal dependence (e.g., Newell et al., 2010). Therefore, given that the DMSP SSJ data are in

677 equally good quality in different seasons, it would be interesting to investigate the seasonal
678 dependance of the differential energy flux in each DMSP SSJ energy channel. Besides, we will
679 include the electron precipitation variability together with its correlation with the electric field
680 variability on different scales, so that the estimation of the localized Joule heating can be
681 improved (Zhu et al., 2018). Moreover, a boundary-oriented binning technique (Zhu et al.,
682 2020a) will be utilized instead of the static-binning method utilized in this study, which can help
683 resolve the smoothing issue caused by the static-binning method and further improve the total
684 Joule heating estimation.

685

686 **7. Summary**

687 In this study, we have developed a new empirical model, ASHLEY, that can improve
688 specifications of the electron precipitation energy spectrum and high-latitude electric field
689 variability in GCMs based on the DMSP electron precipitation and bulk ion drift measurements
690 in the solar cycle 24. In addition to having better consistency between the electron precipitation
691 and electric field, ASHLEY also has several advantages over other existing empirical models,
692 which are summarized as follows:

693 1) The auroral electron precipitation component, ASHLEY-A, provides the averaged
694 differential energy flux in the 19 DMSP energy channels under different IMF and solar wind
695 conditions without making any assumptions about the energy spectrum. It is found that soft
696 electron precipitation specifications can be remarkably improved as compared with the typically
697 assumed Maxwellian energy spectrum having the same total energy flux and average energy.
698 The outputs of ASHLEY-A indicate that the distributions of >500 eV and <500 eV electrons can
699 be significantly different: >500 eV electrons mainly precipitate on the night side whereas <500

700 electrons mainly precipitate on the day side. Moreover, the differential energy flux displays a
 701 salient peak near the local noon in channels with their central energy around 100 eV, which may
 702 correspond to the dayside cusp. Furthermore, the impact of the IMF B_y polarity on the electron
 703 precipitation is better taken into account in ASHLEY-A than existing electron precipitation
 704 models. It is found that the polarity of the IMF B_y component can significantly affect the
 705 distributions of <500 eV electron precipitations.

706 2) ASHLEY provides consistent high-latitude mean electric field and electric field variability
 707 under different IMF and solar wind conditions through ASHLEY-E and ASHLEY-Evar,
 708 respectively. The modeled electric potential and electric field variability distributions are
 709 generally consistent with previous statistical results.

710

711 **Appendix:**

712 **A1. MLT and IMF clock angle fitting**

713 For the differential energy flux (J_E) or σ_1 or σ_2 in each bin of MLAT, ε_t , and θ_c , a fourth-
 714 order Fourier series has been used to capture their MLT variations. Let us call the quantity to be
 715 fitted y , thus:

$$y = \sum_{m=0}^4 (A_m \cos(m\phi) + B_m \sin(m\phi)) \quad (\text{A1})$$

716 Here, $\phi = \frac{\text{MLT}}{12} \pi$, and A_m and B_m are MLT fitting coefficients at the order of m , and are a
 717 function of MLAT, ε_t and θ_c . The maximum order of 4 is determined after trial-and-error tests,
 718 where it has been found that a higher-order Fourier series would not improve the fitting results
 719 yet would introduce unrealistic small-scale structures. For each bin of MLAT and ε_t (median
 720 $\varepsilon_t > 3000$), A_m and B_m are fitted to a fourth-order Fourier series constructed by ω ($\omega = \frac{\theta_c}{180^\circ} \pi$):

$$A_m(\text{or } B_m) = \sum_{n=0}^4 (C_n \cos(n\omega) + D_n \sin(n\omega)) \quad (\text{A2})$$

721 Here, A_m and B_m in each θ_c bin are assumed to represent the fitting coefficients at its central
 722 θ_c , i.e., a multiple of 45° (i.e., a multiple of $\frac{\pi}{4}$ for ω), and in order to implement a fourth-order
 723 fitting, A_m and B_m are linearly interpolated to ω equal to multiples of $\frac{\pi}{8}$. The Fourier fitting is
 724 done using `numpy.linalg.lstsq` in Python's NumPy package (Harris et al., 2020).

725 **A2. Expansions of E_{d1} and E_{d2} in terms of spherical harmonics and electric potential**

726 **fitting**

727 According to Eq. 2 in this paper and Eqs. 4.8 and 4.9 in Richmond (1995), the expansions of
 728 E_{d1} and E_{d2} can be expressed as follows:

$$E_{d1}(\theta, \phi) = \sum_{l=1}^{12} \sum_{m=1}^{\min(l,4)} \frac{m}{R \cos \lambda_m} (F_{lm} \sin m\phi - G_{lm} \cos m\phi) P_l^m(\cos \theta) \quad (\text{A3})$$

729

$$E_{d2}(\theta, \phi) = \frac{4 \sin \theta}{R \sin I_m} \left(\sum_{l=0}^{12} F_{l0} \frac{\partial P_l^0(x)}{\partial x} \Big|_{x=\cos \theta} + \right. \quad (\text{A4})$$

$$\left. \sum_{l=1}^{12} \sum_{m=1}^{\min(l,4)} (F_{lm} \cos m\phi + G_{lm} \sin m\phi) \frac{\partial P_l^m(x)}{\partial x} \Big|_{x=\cos \theta} \right)$$

730 The coefficients in Eqs. A3 and A4 are the same as those in Eq. 2, R in Eqs. A3 and A4 is
 731 6482 (6372+110) km and $\sin I_m$ in Eq. A4 can be calculated by using Eq. 3.7 in Richmond
 732 (1995).

733 By using the electric potential data and their locations, we can construct $\mathbf{A}_1 \mathbf{X} = \mathbf{B}_1$ from Eq 2,
 734 where \mathbf{X} is constructed by F_{lm} and G_{lm} . Similarly, by using E_{d1} and E_{d2} data and their locations,
 735 we can construct $\mathbf{A}_2 \mathbf{X} = \mathbf{B}_2$ and $\mathbf{A}_3 \mathbf{X} = \mathbf{B}_3$ from Eqs. A3 and A4, respectively. The three equations
 736 can further be combined to $\mathbf{A} \mathbf{X} = \mathbf{B}$, where $\mathbf{A}^T = [\mathbf{A}_1^T, \mathbf{A}_2^T, \mathbf{A}_3^T]$ and $\mathbf{B}^T = [\mathbf{B}_1^T, \mathbf{B}_2^T, \mathbf{B}_3^T]$. Similar to

737 the Fourier fitting, we also use `numpy.linalg.lstsq` in Python's NumPy package (Harris et al.,
738 2020) to achieve the fitting.

739 **A3. Reconstruct the electron precipitation pattern for $\varepsilon_t \leq 22770$**

740 Case 1: If $\varepsilon_t \leq 2579$, then the MLT Fourier fitting coefficients in the first ε_t bin are used to
741 reconstruct the differential energy flux in different MLAT bins and energy channels (In this
742 subsection, the ε_t bins correspond to those listed in Table 1a). Case 2: If $\varepsilon_t > 2579$, the two ε_t
743 bins with the median value of ε_t closest to the given ε_t are determined at first by using Table 1a.
744 Then the differential energy flux patterns from those two ε_t bins are combined according to their
745 weights w_1 and w_2 , which can be calculated using following procedures: Assume the closest two
746 median values of ε_t are ε_1 and ε_2 , respectively ($\varepsilon_1 < \varepsilon_t \leq \varepsilon_2$), then $w_1 = \frac{\varepsilon_2 - \varepsilon_t}{\varepsilon_2 - \varepsilon_1}$ and $w_2 = 1 -$
747 w_1 . For the ε_t bin with the median value of ε_t greater than 3000, the MLT fitting coefficients in
748 each MLAT bin and in each channel are reconstructed according to the IMF clock angle Fourier
749 fitting coefficients (determined in Section 3.1.1) and the given IMF clock angle θ_c . Then the
750 differential energy flux is calculated using the MLT Fourier fitting coefficients.

751 **A4. Reconstruct the electric potential and electric field variability patterns for $\varepsilon_t \leq$** 752 **18357**

753 Case 1: If $\varepsilon_t \leq 2583$, then the spherical harmonics fitting coefficients in the first ε_t bin are
754 used to reconstruct the electric potential (In this subsection, the ε_t bins discussed are those listed
755 in Table 1b). Similarly, the MLT Fourier fitting coefficients in different MLAT bins and in the
756 first ε_t bin are used to reconstruct σ_1 and σ_2 in different MLAT bins. Case 2: If $\varepsilon_t > 2583$, the
757 two ε_t bins with the median value of ε_t closest to the given ε_t are determined at first by using
758 Table 1b. Then the patterns from those two ε_t bins are combined according to their weights w_1
759 and w_2 , which can be calculated using following procedures: Assume the closest two median

760 values of ε_t are ε_1 and ε_2 , respectively, then $w_1 = \frac{\beta_2 - \beta}{\beta_2 - \beta_1}$ and $w_2 = 1 - w_1$. Here, β_1 , β_2 and β
761 are calculated from ε_1 , ε_2 and ε_t , respectively ($\varepsilon_1 < \varepsilon_t \leq \varepsilon_2$), using Eq.3 and $\varepsilon_{inf} = 40,000$.
762 For the ε_t bin with the median value of ε_t greater than 3000, the spherical harmonics fitting
763 coefficients are reconstructed according to the IMF clock angle Fourier fitting coefficients
764 determined in Section 3.1.2 and the given IMF clock angle θ_c , and the electric potential can be
765 determined using the spherical harmonics fitting coefficients. Similarly, for the ε_t bin with the
766 median value of ε_t greater than 3000, the MLT Fourier fitting coefficients in each MLAT bin are
767 reconstructed according to the IMF clock angle Fourier fitting coefficients determined in Section
768 3.1.3 and the given IMF clock angle θ_c . Then σ_1 and σ_2 in different MLAT bins can be
769 determined using the MLT Fourier fitting coefficients.

770 **A5. Variables defined in Sections 2-5**

771 Table 2 lists all variables defined in Sections 2-5, including their definitions, units, calculations
772 and places of first shown, for better references.

773

774 **Acknowledgements:** The research at University of Texas at Arlington (UTA) was supported
775 by AFOSR through award FA9559-16-1-0364 and NASA 80NSSC20K0195. AM was supported
776 by AFOSR through award FA9550-17-1-0248. DJK and LMK were supported by AFOSR
777 through awards FA9550-17-1-0258 and FA9559-16-1-0364. This material is based upon work
778 supported by the National Center for Atmospheric Research, which is a major facility sponsored
779 by the National Science Foundation under Cooperative Agreement No. 1852977. The authors
780 thank Arthur Richmond for his helpful comments on the manuscript and acknowledge use of
781 NASA/GSFC's Space Physics Data Facility's OMNIWeb (or CDAWeb or ftp) service, and
782 OMNI data. The IMF and solar wind data can be downloaded from NASA SPDF OMNIWeb

783 (<https://omniweb.gsfc.nasa.gov>). The DMSP electron precipitation and auroral boundary data
784 can be found at NASA SPDF CDAWeb (<https://cdaweb.sci.gsfc.nasa.gov/index.html/>) and the
785 DMSP ion drift data can be obtained at NOAA NCEI (<https://satdat.ngdc.noaa.gov/dmsp/data/>).
786 The codes of auroral boundary identification technique developed by Kilcommons et al. (2017)
787 are available at Kilcommons and Burrell (2019) and the link is
788 <http://doi.org/10.5281/zenodo.3267415>. The data used to generate the figures are available at
789 Zhu et al., (2020b) and the link is <http://doi.org/10.5281/zenodo.4151717>. The codes of
790 ASHLEY are available at Zhu et al., (2020c) and the link is
791 <https://doi.org/10.5281/zenodo.4152364>.

792

793

794 **References**

- 795 Billett, D. D., Grocott, A., Wild, J. A., Walach, M. T., & Kosch, M. J. (2018). Diurnal variations
796 in global Joule heating morphology and magnitude due to neutral winds. *Journal of Geophysical*
797 *Research: Space Physics*, 123, 2398–2411. <https://doi.org/10.1002/2017JA025141>
798
- 799 Buonsanto, M. J. (1999). Ionospheric Storms—A Review. *Space Science Reviews*, 88(3), 563–
800 601. <https://doi.org/10.1023/A:1005107532631>
801
- 802 Burleigh, M., Zettergren, M., Lynch, K., Lessard, M., Moen, J., Clausen, L., Kenward, D.,
803 Hysell, D., & Liemohn, M. (2019). Transient Ionospheric Upflow Driven by Poleward Moving
804 Auroral forms Observed During the Rocket Experiment for Neutral Upwelling 2 (RENU2)
805 Campaign. *Geophysical Research Letters*, 46(12), 6297–6305.
806 <https://doi.org/10.1029/2018GL081886>
807
- 808 Candidi, M., H. W. Kroehl, and C. I. Meng (1983), Intensity distribution of dayside polar soft
809 electron precipitation and the IMF, *Planetary and Space Science*, 31(5), 489–498,
810 doi:10.1016/0032-0633(83)90040-5.
811
- 812 Cole, K. D. (1962). Joule heating of the upper atmosphere. *Australian Journal of Physics*, 15,
813 223.
814
- 815 Codrescu, M. V., T. J. Fuller-Rowell, and J. C. Foster (1995), On the importance of E-field
816 variability for Joule heating in the high-latitude thermosphere, *Geophys. Res. Lett.*, 22, 2393–
817 2396, doi: 10.1029/95GL01909.
818
- 819 Codrescu, M. V., T. J. Fuller-Rowell, J. C. Foster, J. M. Holt, and S. J. Cariglia (2000), Electric
820 field variability associated with the Millstone Hill electric field model, *J. Geophys. Res.*,
821 105(A3), 5265–5274, doi:10.1029/1999JA900463.
822
- 823 Codrescu, M. V., T. J. Fuller-Rowell, V. Munteanu, C. F. Minter, and G. H. Millward (2008),
824 Validation of the Coupled Thermosphere Ionosphere Plasmasphere Electrodynamics model:
825 CTIPE-Mass Spectrometer Incoherent Scatter temperature comparison, *Space Weather*, 6(9),
826 09005, doi:10.1029/2007SW000364.
827
- 828 Cosgrove, R. B., and J. P. Thayer (2006), Parametric dependence of electric field variability in
829 the sondrestrom database: A linear relation with k_p , *Journal of Geophysical Research: Space*
830 *Physics*, 111(A10), doi:10.1029/2006JA011658.
831
- 832 Cosgrove, R. B., & Codrescu, M. (2009). Electric field variability and model uncertainty: A
833 classification of source terms in estimating the squared electric field from an electric field model.
834 *Journal of Geophysical Research: Space Physics*, 114(A6).
835 <https://doi.org/10.1029/2008JA013929>
836
- 837 Cosgrove, R., M. McCready, R. Tsunoda, and A. Stromme (2011), The bias on the joule heating
838 estimate: Small-scale variability versus resolved-scale model uncertainty and the correlation of

839 electric field and conductance, *Journal of Geophysical Research: Space Physics*, 116(A9),
840 doi:10.1029/2011JA016665.

841

842 Cousins, E. D. P., and S. G. Shepherd (2010), A dynamical model of high-latitude convection
843 derived from SuperDARN plasma drift measurements, *J. Geophys. Res.*, 115, A12329,
844 doi:10.1029/2010JA016017.

845

846 Cousins, E. D. P., and S. G. Shepherd (2012), Statistical maps of small-scale electric field
847 variability in the high-latitude ionosphere, *Journal of Geophysical Research (Space Physics)*,
848 117(A12), A12304, doi:10.1029/2012JA017929.

849

850 Crowley, G., & Hackert, C. L. (2001). Quantification of high latitude electric field variability.
851 *Geophysical Research Letters*, 28(14), 2783–2786. <https://doi.org/10.1029/2000GL012624>

852

853 Deng, Y., Maute, A., Richmond, A. D., and Roble, R. G. (2008), Analysis of thermospheric
854 response to magnetospheric inputs, *J. Geophys. Res.*, 113, A04301, doi:10.1029/2007JA012840.

855

856 Deng, Y., A. Maute, A. D. Richmond, and R. G. Roble (2009), Impact of electric field variability
857 on Joule heating and thermospheric temperature and density, *Geophys. Res. Lett.*, 36, L08105,
858 doi: 10.1029/2008GL036916.

859

860 Deng, Y., T. J. Fuller-Rowell, R. A. Akmaev, and A. J. Ridley (2011), Impact of the altitudinal
861 Joule heating distribution on the thermosphere, *Journal of Geophysical Research (Space*
862 *Physics)*, 116, A05313, doi:10.1029/2010JA016019.

863

864 Emery, B. A., Lathuillere, C., Richards, P. G., Roble, R. G., Buonsanto, M. J., Knipp, D. J., et al.
865 (1999). Time dependent thermospheric neutral response to the 2–11 November 1993 storm
866 period. *Journal of Atmospheric and Terrestrial Physics*, 61(3-4), 329–350. [https://doi.org/](https://doi.org/10.1016/S1364-6826(98)00137-0)
867 [10.1016/S1364-6826\(98\)00137-0](https://doi.org/10.1016/S1364-6826(98)00137-0).

868

869 Evans, D. S. (1974), Precipitating electron fluxes formed by a magnetic field aligned potential
870 difference, *J. Geophys. Res.*, 79(19), 2853, doi:10.1029/JA079i019p02853.

871

872 Evans, D. S., and T. E. Moore (1979), Precipitating electrons associated with the diffuse aurora:
873 evidence for electrons of atmospheric origin in the plasma sheet, *J. Geophys. Res.*, 84(A11),
874 6451–6457, doi:10.1029/JA084iA11p06451.

875

876 Fedrizzi, M., Fuller-Rowell, T. J., & Codrescu, M. V. (2012). Global Joule heating index derived
877 from thermospheric density physics-based modeling and observations. *Space Weather*, 10(3).
878 <https://doi.org/10.1029/2011SW000724>

879

880 Feldstein, Y. I., & Starkov, G. V. (1967). Dynamics of auroral belt and polar geo magnetic
881 disturbances. *Planetary and Space Science*, 15, 209–229. [https://doi.org/10.1016/0032-](https://doi.org/10.1016/0032-0633(67)90190-0)
882 [0633\(67\)90190-0](https://doi.org/10.1016/0032-0633(67)90190-0)

883

884 Fuller-Rowell, T. J., and D. S. Evans (1987), Height-integrated Pedersen and Hall conductivity

885 patterns inferred from the TIROS-NOAA satellite data, *J. Geophys. Res.*, 92, 7606–7618, doi:
886 10.1029/JA092iA07p07606.

887

888 Fuller-Rowell, T. J., Codrescu, M. V., Moffett, R. J., & Quegan, S. (1994). Response of the
889 thermosphere and ionosphere to geomagnetic storms. *Journal of Geophysical Research: Space*
890 *Physics*, 99(A3), 3893–3914. <https://doi.org/10.1029/93JA02015>

891

892 Fuller-Rowell, T. J., Codrescu, M. C., and Wilkinson, P.: Quantitative modeling of the
893 ionospheric response to geomagnetic activity, *Ann. Geophys.*, 18, 766–781,
894 <https://doi.org/10.1007/s00585-000-0766-7>, 2000.

895

896 Fung, S. F., and R. A. Hoffman (1988), On the spectrum of the secondary auroral electrons, *J.*
897 *Geophys. Res.*, 93(A4), 2715–2724, doi:10.1029/JA093iA04p02715.

898

899 Hairston, M. R., K. A. Drake, and R. Skoug (2005), Saturation of the ionospheric polar cap
900 potential during the October-November 2003 superstorms, *Journal of Geophysical Research*
901 *(Space Physics)*, 110(A9), A09S26, doi:10.1029/2004JA010864.

902

903 Hardy, D. A., M. S. Gussenhoven, and E. Holeman (1985), A statistical model of auroral
904 electron precipitation, *J. Geophys. Res.*, 90(A5), 4229–4248, doi: 10.1029/JA090iA05p04229.

905

906 Hardy, D. A., Gussenhoven, M. S., Raistrick, R., & McNeil, W. J. (1987). Statistical and
907 functional representations of the pattern of auroral energy flux, number flux, and conductivity.
908 *Journal of Geophysical Research: Space Physics*, 92(A11), 12275–12294.
909 <https://doi.org/10.1029/JA092iA11p12275>

910

911 Hardy, D. A., Holeman, E. G., Burke, W. J., Gentile, L. C., & Bounar, K. H. (2008). Probability
912 distributions of electron precipitation at high magnetic latitudes. *Journal of Geophysical*
913 *Research: Space Physics*, 113(A6). <https://doi.org/10.1029/2007JA012746>

914

915 Harris, C.R., Millman, K.J., van der Walt, S.J. et al. Array programming with NumPy. *Nature*
916 585, 357–362 (2020). DOI: [0.1038/s41586-020-2649-2](https://doi.org/10.1038/s41586-020-2649-2).

917

918 Heelis, R. A., Lowell, J. K., & Spiro, R. W. (1982). A model of the high-latitude ionospheric
919 convection pattern. *Journal of Geophysical Research: Space Physics*, 87(A8), 6339–6345.
920 <https://doi.org/10.1029/JA087iA08p06339>

921

922 Hogan, B., Lotko, W., & Pham, K. (2020). Alfvénic Thermospheric Upwelling in a Global
923 Geospace Model. *Journal of Geophysical Research: Space Physics*, 125(12), e2020JA028059.
924 <https://doi.org/10.1029/2020JA028059>

925

926 Huang, Y., Richmond, A. D., Deng, Y., and Roble, R. (2012), Height distribution of Joule
927 heating and its influence on the thermosphere, *J. Geophys. Res.*, 117, A08334,
928 doi:10.1029/2012JA017885.

929

930 Jackson, J. D. (2007), *Classical electrodynamics*, John Wiley & Sons.

931
932 Khazanov, G. V., Glocer, A., & Himwich, E. W. (2014). Magnetosphere-ionosphere energy
933 interchange in the electron diffuse aurora. *Journal of Geophysical Research: Space Physics*,
934 119(1), 171–184. <https://doi.org/10.1002/2013JA019325>
935
936 Khazanov, G. V., & Glocer, A. (2020). How Magnetically Conjugate Atmospheres and the
937 Magnetosphere Participate in the Formation of Low-Energy Electron Precipitation in the Region
938 of Diffuse Aurora. *Journal of Geophysical Research: Space Physics*, 125(8), e2020JA028057.
939
940 Kilcommons, L. M., R. J. Redmon, and D. J. Knipp (2017), A new DMSP magnetometer and
941 auroral boundary data set and estimates of field-aligned currents in dynamic auroral boundary
942 coordinates, *J. Geophys. Res. Space Physics*, 122, 9068–9079, doi:10.1002/2016JA023342.
943
944 Kilcommons, L. M, and A. G. Burrell (2019). `lkilcommons/ssj_auroral_boundary`: Version 1
945 (Version v1.0.0). Zenodo. <http://doi.org/10.5281/zenodo.3267415>
946
947 Laundal, K.M., Richmond, A.D. Magnetic Coordinate Systems. *Space Sci Rev* 206, 27–59
948 (2017). <https://doi-org/10.1007/s11214-016-0275-y>
949
950 Liemohn, M. W. (2020). The Case for Improving the Robinson Formulas. *Journal of*
951 *Geophysical Research: Space Physics*, 125(10), e2020JA028332.
952 <https://doi.org/10.1029/2020JA028332>
953
954 Lotko, W., & Zhang, B. (2018). Alfvénic Heating in the Cusp Ionosphere-Thermosphere. *Journal*
955 *of Geophysical Research: Space Physics*, 123(12), 10,368-10,383.
956 <https://doi.org/10.1029/2018JA025990>
957
958 Lu, G., A. D. Richmond, B. A. Emery, and R. G. Roble (1995), Magnetosphere-ionosphere-
959 thermosphere coupling: Effect of neutral winds on energy transfer and field-aligned current, *J.*
960 *Geophys. Res.*, 100, 19,643–19,660, doi:10.1029/95JA00766.
961
962 Lu, G., A. D. Richmond, H. Lühr, and L. Paxton (2016), High-latitude energy input and its
963 impact on the thermosphere, *Journal of Geophysical Research (Space Physics)*, 121(7), 7108–
964 7124, doi:10.1002/2015JA022294.
965
966 Lu, G., Zakharenkova, I., Cherniak, I., & Dang, T. (2020). Large-Scale Ionospheric Disturbances
967 During the 17 March 2015 Storm: A Model-Data Comparative Study. *Journal of Geophysical*
968 *Research: Space Physics*, 125(5), e2019JA027726. <https://doi.org/10.1029/2019JA027726>
969
970 Matsuo, T., A. D. Richmond, and K. Hensel (2003), High-latitude ionospheric electric field
971 variability and electric potential derived from DE-2 plasma drift measurements: Dependence on
972 IMF and dipole tilt, *Journal of Geophysical Research (Space Physics)*, 108, 1005,
973 doi:10.1029/2002JA009429
974
975 Matsuo, T., & Richmond, A. D. (2008). Effects of high-latitude ionospheric electric field
976 variability on global thermospheric Joule heating and mechanical energy transfer rate. *Journal of*

977 Geophysical Research: Space Physics, 113(A7). <https://doi.org/10.1029/2007JA012993>
978
979 Merkin, V. G., and C. C. Goodrich (2007), Does the polar cap area saturate? *Geophys. Res. Lett.*,
980 34(9), L09107, doi:10.1029/2007GL029357.
981
982 McIntosh, R. C., & Anderson, P. C. (2014). Maps of precipitating electron spectra characterized
983 by Maxwellian and kappa distributions. *Journal of Geophysical Research: Space Physics*,
984 119(12), 10,116-10,132. <https://doi.org/10.1002/2014JA020080>
985
986 Meier, R. R., D. J. Strickland, J. H. Hecht, and A. B. Christensen (1989), Deducing composition
987 and incident electron spectra from ground-based auroral optical measurements: A study of
988 auroral red line processes, *J. Geophys. Res.*, 94(A10), 13,541–13,552, doi:
989 10.1029/JA094iA10p13541.
990
991 Mitchell, E. J., R. E. Lopez, R. J. Bruntz, M. Wiltberger, J. G. Lyon, R. C. Allen, S. J. Cockrell,
992 and P. L. Whittlesey (2010), Saturation of transpolar potential for large Y component
993 interplanetary magnetic field, *Journal of Geophysical Research (Space Physics)*, 115(A6),
994 A06201, doi:10.1029/2009JA015119.
995
996 Newell, P. T., and C.-I. Meng (1988), The cusp and the cleft/boundary layer: Low-altitude
997 identification and statistical local time variation, *J. Geophys. Res.*, 93(A12), 14,549– 14,556,
998 doi:10.1029/JA093iA12p14549.
999
1000 Newell, P. T., C.-I. Meng, D. G. Sibeck, and R. Lepping (1989), Some low-altitude cusp
1001 dependencies on the interplanetary magnetic field, *J. Geophys. Res.*, 94(A7), 8921–8927,
1002 doi:10.1029/JA094iA07p08921.
1003
1004 Newell, P. T., and C.-I. Meng (1994), Ionospheric projections of magnetospheric regions under
1005 low and high solar wind pressure conditions, *J. Geophys. Res.*, 99(A1), 273–286,
1006 doi:10.1029/93JA02273.
1007
1008 Newell, P. T., Ruohoniemi, J. M., & Meng, C.-I. (2004). Maps of precipitation by source region,
1009 binned by IMF, with inertial convection streamlines. *Journal of Geophysical Research: Space*
1010 *Physics*, 109(A10). <https://doi.org/10.1029/2004JA010499>
1011
1012 Newell, P. T., T. Sotirelis, K. Liou, C. I. Meng, and F. J. Rich (2007), A nearly universal solar
1013 wind-magnetosphere coupling function inferred from 10 magnetospheric state variables, *Journal*
1014 *of Geophysical Research (Space Physics)*, 112(A1), A01206, doi: 10.1029/2006JA012015.
1015
1016 Newell, P. T., T. Sotirelis, K. Liou, and F. J. Rich (2008), Pairs of solar wind-magnetosphere
1017 coupling functions: Combining a merging term with a viscous term works best, *Journal of*
1018 *Geophysical Research (Space Physics)*, 113(A4), A04218, doi: 10.1029/2007JA012825.
1019
1020 Newell, P. T., T. Sotirelis, and S. Wing (2009), Diffuse, monoenergetic, and broadband aurora:
1021 The global precipitation budget, *J. Geophys. Res.*, 114, A09207, doi:10.1029/2009JA014326.
1022

1023 Newell, Patrick T., Sotirelis, T., & Wing, S. (2010). Seasonal variations in diffuse,
1024 monoenergetic, and broadband aurora. *Journal of Geophysical Research: Space Physics*,
1025 115(A3). <https://doi.org/10.1029/2009JA014805>
1026

1027 Newell, P. T., Liou, K., Zhang, Y., Sotirelis, T., Paxton, L. J., & Mitchell, E. J. (2014).
1028 OVATION Prime-2013: Extension of auroral precipitation model to higher disturbance levels.
1029 *Space Weather*, 12(6), 368–379. <https://doi.org/10.1002/2014SW001056>
1030

1031 Papitashvili, V. O., and F. J. Rich (2002), High-latitude ionospheric convection models derived
1032 from Defense Meteorological Satellite Program ion drift observations and parameterized by the
1033 interplanetary magnetic field strength and direction, *Journal of Geophysical Research (Space*
1034 *Physics)*, 107(A8), 1198, doi:10.1029/2001JA000264.
1035

1036 Pedatella, N. M., Lu, G., & Richmond, A. D. (2018). Effects of high-latitude forcing uncertainty
1037 on the low-latitude and midlatitude ionosphere. *Journal of Geophysical Research: Space Physics*,
1038 123, 862–882. <https://doi.org/10.1002/2017JA024683>
1039

1040 Pröls, G. W. (2011). Density Perturbations in the Upper Atmosphere Caused by the Dissipation
1041 of Solar Wind Energy. *Surveys in Geophysics*, 32(2), 101–195. [https://doi.org/10.1007/s10712-](https://doi.org/10.1007/s10712-010-9104-0)
1042 [010-9104-0](https://doi.org/10.1007/s10712-010-9104-0)
1043

1044 Rees, M. H. (1989). *Physics and chemistry of the upper atmosphere (Vol. 1)*. Cambridge
1045 University Press.
1046

1047 Redmon, R. J., W. F. Denig, L. M. Kilcommons, and D. J. Knipp (2017), New DMSP database
1048 of precipitating auroral electrons and ions, *J. Geophys. Res. Space Physics*, 122, 9056–9067,
1049 doi:10.1002/2016JA023339.
1050

1051 Richards, P. G. (2013), Reevaluation of thermosphere heating by auroral electrons, *Advances in*
1052 *Space Research*, 51(4), 610–619, doi:10.1016/j.asr.2011.09.004.
1053

1054 Richmond, A. D., and Y. Kamide (1988), Mapping electrodynamic features of the high-latitude
1055 ionosphere from localized observations: Technique, *J. Geophys. Res.*, 93(A6), 5741–5759,
1056 doi:10.1029/JA093iA06p05741.
1057

1058 Richmond, A. D. (1992), Assimilative mapping of ionospheric electrodynamics, *Advances*
1059 *in Space Research*, 12(6), 59–68, doi:10.1016/0273-1177(92)90040-5.
1060

1061 Richmond, A. D. (1995), Ionospheric Electrodynamics Using Magnetic Apex Coordinates.,
1062 *Journal of Geomagnetism and Geoelectricity*, 47(2), 191–212, doi:10.5636/jgg.47.191.
1063

1064 Richmond, A.D. (accepted). Joule heating in the thermosphere. In W. Wang, Y. Zhang (Eds.),
1065 *Advances in Upper Atmosphere Research: Dynamics and Energetics*. Washington, DC:
1066 American Geophysical Union.
1067

1068 Ridley, A. J., and E. A. Kihn (2004), Polar cap index comparisons with AMIE cross polar cap

1069 potential, electric field, and polar cap area, *Geophys. Res. Lett.*, 31(7), L07801, doi:
1070 10.1029/2003GL019113.

1071

1072 Robinson, R. M., Vondrak, R. R., Miller, K., Dabbs, T., & Hardy, D. (1987). On calculating
1073 ionospheric conductances from the flux and energy of precipitating electrons. *Journal of*
1074 *Geophysical Research: Space Physics*, 92(A3), 2565–2569.
1075 <https://doi.org/10.1029/JA092iA03p02565>

1076

1077 Roble, R. G., & Ridley, E. C. (1987). An auroral model for the NCAR thermospheric general
1078 circulation model (TGCM). *AnGeo*, 5, 369-382.

1079

1080 Rodger, A. S., Wells, G. D., Moffett, R. J., & Bailey, G. J. (2001). The variability of Joule
1081 heating, and its effects on the ionosphere and thermosphere. *Annales Geophysicae*, 19(7), 773–
1082 781. <https://doi.org/10.5194/angeo-19-773-2001>

1083

1084 Sheng, C., Deng, Y., Chen, Y.-J., Heelis, R. A., & Huang, Y. (2019). Effects of Alignment
1085 Between Particle Precipitation and Ion Convection Patterns on Joule Heating. *Journal of*
1086 *Geophysical Research: Space Physics*, 124(6), 4905–4915.
1087 <https://doi.org/10.1029/2018JA026446>

1088

1089 Shepherd, S. G. (2007). Polar cap potential saturation: Observations, theory, and modeling.
1090 *Journal of Atmospheric and Solar-Terrestrial Physics*, 69(3), 234–248.
1091 <https://doi.org/10.1016/j.jastp.2006.07.022>

1092

1093 Sotirelis, T., J. M. Ruohoniemi, R. J. Barnes, P. T. Newell, R. A. Greenwald, J. P. Skura, and C.-
1094 I. Meng (2005), Comparison of SuperDARN radar boundaries with DMSP particle precipitation
1095 boundaries, *J. Geophys. Res.*, 110, A06302, doi:10.1029/2004JA010732.

1096

1097 Strickland, D. J., J. Daniell, R. E., J. R. Jasperse, and B. Basu (1993), Transport-theoretic model
1098 for the electron-proton-hydrogen atom aurora 2. Model results, *J. Geophys. Res.*, 98(A12),
1099 21,533–21,548, doi:10.1029/93JA01645.

1100

1101 Thayer, J. P. (2000). High-latitude currents and their energy exchange with the ionosphere-
1102 thermosphere system. *Journal of Geophysical Research: Space Physics*, 105(A10), 23015–
1103 23024. <https://doi.org/10.1029/1999JA000409>

1104

1105 Thébault, E., Finlay, C. C., Beggan, C. D., Alken, P., Aubert, J., Barrois, O., Bertrand, F.,
1106 Bondar, T., Boness, A., Brocco, L., Canet, E., Chambodut, A., Chulliat, A., Coisson, P., Civet,
1107 F., Du, A., Fournier, A., Fratter, I., Gillet, N., ... Zvereva, T. (2015). International Geomagnetic
1108 Reference Field: The 12th generation. *Earth, Planets and Space*, 67(1), 79.
1109 <https://doi.org/10.1186/s40623-015-0228-9>

1110

1111 Thomas, E. G., & Shepherd, S. G. (2018). Statistical Patterns of Ionospheric Convection Derived
1112 From Mid-latitude, High-Latitude, and Polar SuperDARN HF Radar Observations. *Journal of*
1113 *Geophysical Research: Space Physics*, 123(4), 3196–3216.
1114 <https://doi.org/10.1002/2018JA025280>

1115
1116 Verkhoglyadova, O. P., Meng, X., Mannucci, A. J., & McGranaghan, R. M. (2018).
1117 Semianalytical Estimation of Energy Deposition in the Ionosphere by Monochromatic Alfvén
1118 Waves. *Journal of Geophysical Research: Space Physics*, 123(6), 5210–5222.
1119 <https://doi.org/10.1029/2017JA025097>
1120
1121 Vickrey, J. F., Vondrak, R. R., & Matthews, S. J. (1981). The diurnal and latitudinal variation of
1122 auroral zone ionospheric conductivity. *Journal of Geophysical Research: Space Physics*, 86(A1),
1123 65–75. <https://doi.org/10.1029/JA086iA01p00065>
1124
1125 Weimer, D. R. (1995), Models of high-latitude electric potentials derived with a least error fit of
1126 spherical harmonic coefficients, *J. Geophys. Res.*, 100(A10), 19,595–19,608, doi:
1127 10.1029/95JA01755.
1128
1129 Weimer, D. R. (2005), Improved ionospheric electrodynamic models and application to
1130 calculating Joule heating rates, *Journal of Geophysical Research (Space Physics)*, 110, A05306,
1131 doi: 10.1029/2004JA010884.
1132
1133 Wilder, F. D., C. R. Clauer, and J. B. H. Baker (2008), Reverse convection potential saturation
1134 during northward IMF, *Geophys. Res. Lett.*, 35(12), L12103, doi: 10.1029/2008GL034040.
1135
1136 Wing, S., Khazanov, G. V., Sibeck, D. G., & Zesta, E. (2019). Low Energy Precipitating
1137 Electrons in the Diffuse Aurorae. *Geophysical Research Letters*, 46(7), 3582–3589.
1138 <https://doi.org/10.1029/2019GL082383>
1139
1140 Zhang, B., Lotko, W., Brambles, O., Wiltberger, M., & Lyon, J. (2015). Electron precipitation
1141 models in global magnetosphere simulations. *Journal of Geophysical Research: Space Physics*,
1142 120(2), 1035–1056. <https://doi.org/10.1002/2014JA020615>
1143
1144 Zhang, Y., and L. J. Paxton (2008), An empirical Kp-dependent global auroral model based on
1145 TIMED/GUVI FUV data, *Journal of Atmospheric and Solar-Terrestrial Physics*, 70, 1231–1242,
1146 doi: 10.1016/j.jastp.2008.03.008.
1147
1148 Zhu, Q., Deng, Y., Richmond, A., & Maute, A. (2018). Small-Scale and Mesoscale Variabilities
1149 in the Electric Field and Particle Precipitation and Their Impacts on Joule Heating. *Journal of*
1150 *Geophysical Research: Space Physics*, 123(11), 9862–9872.
1151 <https://doi.org/10.1029/2018JA025771>
1152
1153 Zhu, Q., Deng, Y., Richmond, A., Maute, A., Chen, Y. J., Hairston, M., ... & Mitchell, E.
1154 (2020a). Impacts of Binning Methods on High-Latitude Electrodynamic Forcing: Static Versus
1155 Boundary-Oriented Binning Methods. *Journal of Geophysical Research: Space Physics*, 125(1),
1156 e2019JA027270.
1157
1158 Zhu, Qingyu, Deng, Yue, Maute, Astrid, Kilcommons, Liam, Knipp, Delores, & Hairston, Marc.
1159 (2020b). ASHLEY: A new empirical model for the high-latitude electron precipitation and
1160 electric field (Version V1). <http://doi.org/10.5281/zenodo.4151717>.

1161
1162 Zhu, Qingyu, Deng, Yue, Maute, Astrid, Kilcommons, Liam, Knipp, Delores, & Hairston, Marc.
1163 (2020c). qyzhuta/ASHLEY_v1: beta (Version v1). Zenodo.
1164 <https://doi.org/10.5281/zenodo.4152364>.

1165 **Tables and Figures**

1166

1167 Table 1a. Electron precipitation

	1	2	3	4	5	6	7	8	9
Lower boundary	0	3000	5000	7000	9000	11000	13000	16000	20000
Upper boundary	3000	5000	7000	9000	11000	13000	16000	20000	30000
Median	2579	4283	6073	7956	9930	11942	14254	17590	22770

1168

1169

1170 Table 1b. Electric field/potential

	1	2	3	4	5	6	7
Lower boundary	0	3000	5500	7500	9500	12000	16000
Upper boundary	3000	5500	7500	9500	12000	16000	24000
Median	2583	4615	6539	8456	10614	13524	18357

1171

1172 Table 1. Summary of the lower and upper boundaries along with the median value of each ε_t bin
 1173 used in binning (a) the electron precipitation and (b) electric field/potential data.

1174

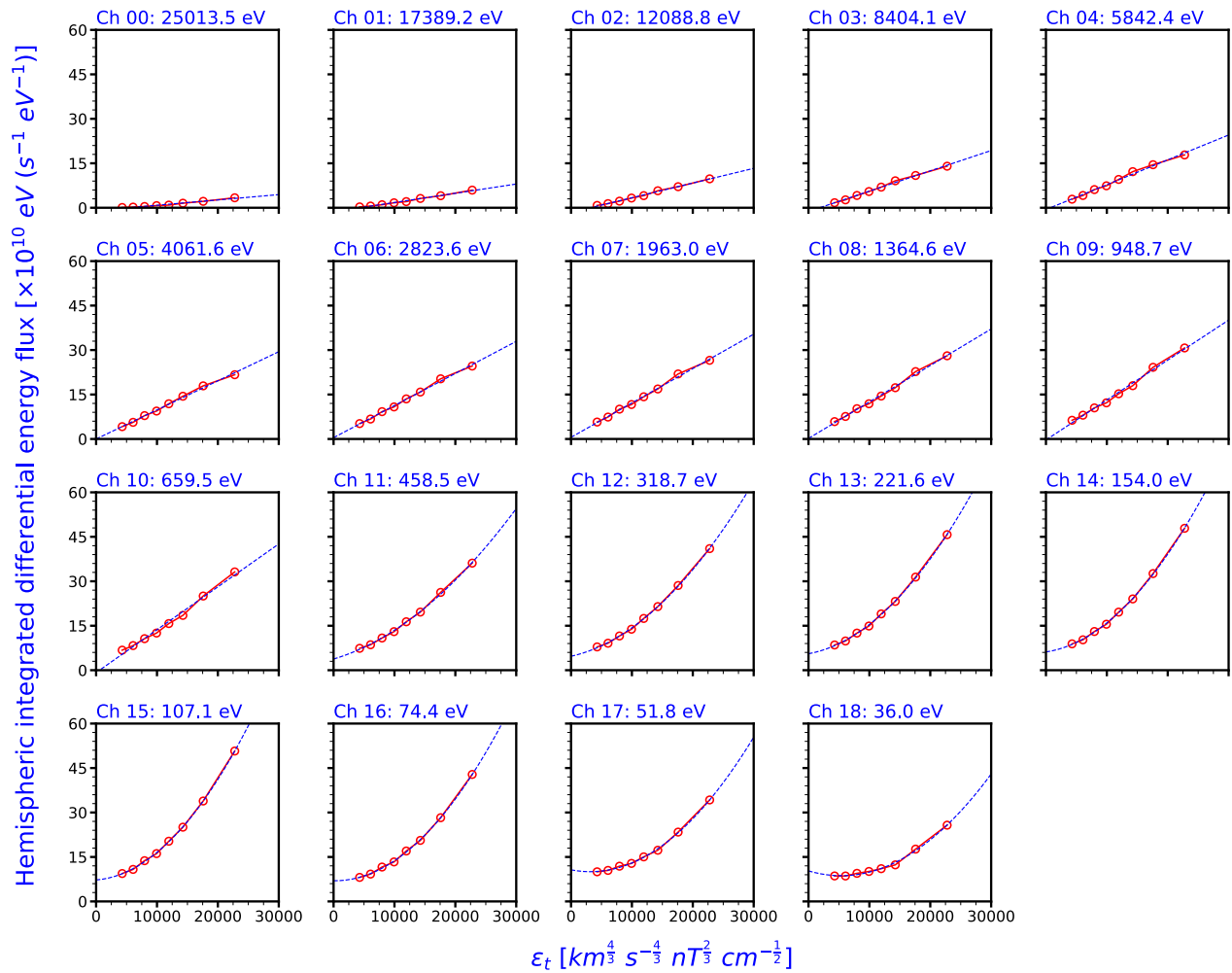
1175

Variable(s)	Meaning	Unit	Calculation	First shown
\mathbf{V} (\mathbf{V}')	bulk ion drift vector before (after) baseline correction	m/s	–	Section 2.1
V_x, V_y, V_z (V'_x, V'_y, V'_z)	Components of \mathbf{V} (\mathbf{V}') in the spacecraft coordinate system	m/s	–	Section 2.1
\mathbf{B}_0, B_{0z}	Background geomagnetic main field vector and its vertical component at the satellite location, respectively	nT	–	Section 2.1
\mathbf{E}	Electric field vector	mV/m	$-\mathbf{V}' \times \mathbf{B}_0$	Section 2.1
E_x	Along-track electric field component	mV/m	$\approx -V'_y B_{0z}$	Section 2.1
B_y, B_z	IMF y and z components in the GSM coordinates	nT	–	Section 2.2
B_T	IMF transverse component magnitude	nT	$\sqrt{B_y^2 + B_z^2}$	Section 2.2
θ_c	IMF clock angle	degree	$\text{atan2}(B_y, B_z)$	Section 2.2
V_{sw}, N_{sw}	Solar wind flow speed and proton density, respectively	km/s, cm^{-3}	–	Section 2.2
ε_t	Coupling function	$(\text{km}^{4/3} \text{s}^{-4/3} \text{nT}^{2/3} \text{cm}^{-1/2})$	$V_{sw}^{4/3} B_T^{2/3} N_{sw}^{1/6}$	Section 2.3
J_E	Differential energy flux	$\text{eV}/(\text{cm}^{-2} \text{s}^{-1} \text{sr}^{-1} \text{eV}^{-1})$	–	Section 3.1.1
ϕ	Azimuthal angle	radian	$\frac{\text{MLT}}{12} \pi$	Section 3.1.1
ω	IMF clock angle in radians	radian	$\frac{\theta_c}{180^\circ} \pi$	Section 3.1.1
Φ	Electric potential	kV	–	Section 3.1.2
λ_m	MLAT in radians	radian	–	Section 3.1.2

θ	Polar angle	radian	$\frac{\pi}{2} - \lambda_m$ $\frac{\pi}{4}$	Section 3.1.2
E_{d1}, E_{d2}	Electric field components in \mathbf{d}_1 and \mathbf{d}_2 directions (Richmond, 1995)	mV/m	–	Section 3.1.2
E'_{d1}, E'_{d2}	Residuals between the measured and modeled E_{d1} and E_{d2} , respectively	mV/m	–	Section 3.1.3
σ_1, σ_2	Standard deviation of E'_{d1} and E'_{d2} , respectively	mV/m	–	Section 3.1.3
Φ_{PC}	Cross-polar-cap potential	kV	–	Section 3.2.1.2
ϵ_{inf}	Saturation level of ϵ_t	$(\text{km}^{4/3} \text{ s}^{-4/3}$ $\text{nT}^{2/3} \text{ cm}^{-1/2})$	–	Section 3.2.1.2
β	Saturation factor	–	$\frac{\epsilon_t}{\sqrt{1 + \left(\frac{\epsilon_t}{\epsilon_{inf}}\right)^2}}$	Section 3.2.1.2
r	Averaged co-MLAT of the boundary identified on dawn and dusk sides	degree	–	Section 3.2.1.2
Q_0, \bar{E}	Total energy flux and average energy, respectively	mW/m ² , eV	Eq. 2 in Robinson et al. (1987)	Section 5.1
$\bar{E}_{d1}, \bar{E}_{d2}$	E_{d1} and E_{d2} calculated from Φ , respectively	mV/m	Eqs. 4.8 and 4.9 in Richmond (1995)	Section 5.2
E_1	Mean electric field magnitude	mV/m	$\sqrt{\bar{E}_{d1}^2 + \bar{E}_{d2}^2}$	Section 5.2
E_2	Electric field variability magnitude	mV/m	$\sqrt{\sigma_1^2 + \sigma_2^2}$	Section 5.2

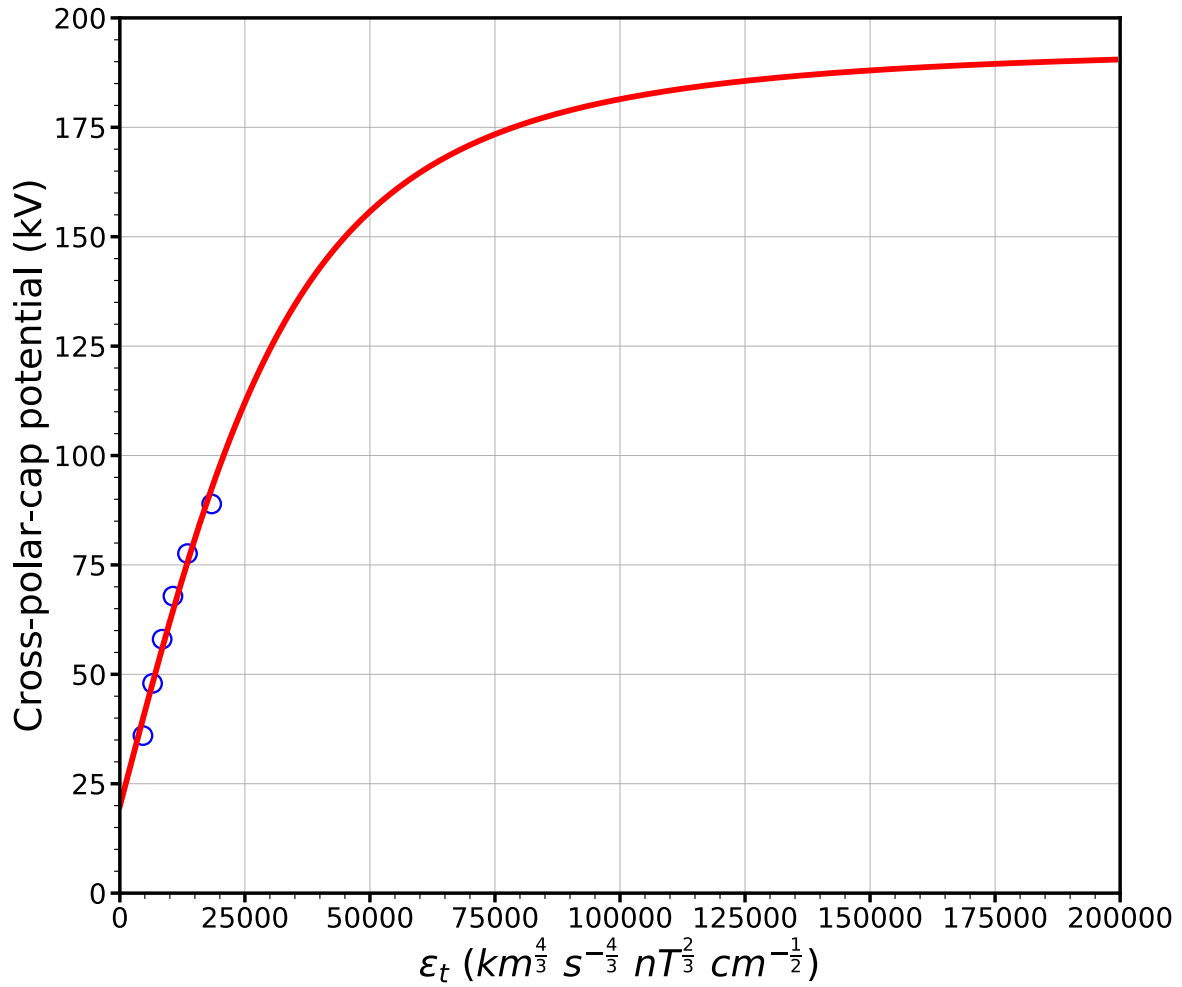
1176
1177
1178
1179

Table 2. Summary of variables defined in Sections 2-5.



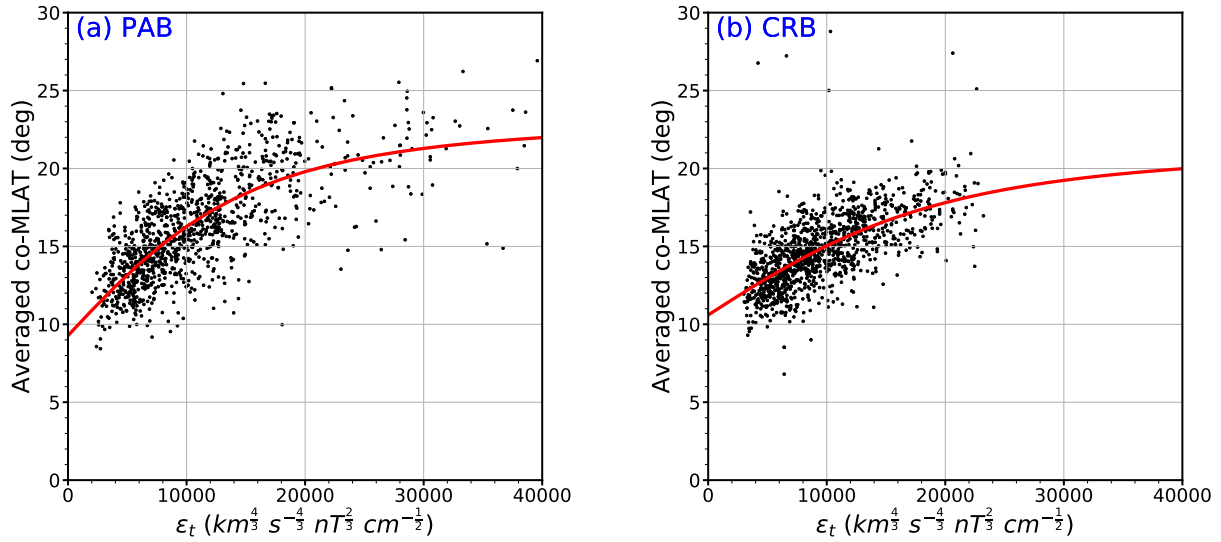
1180
 1181
 1182
 1183
 1184
 1185

Figure 1. Hemispheric-integrated differential energy fluxes in the 19 DMSP energy channels from all 8 ε_t - θ_c bins for the ASHLEY-A development where θ_c is centered at 225° . The blue dashed lines represent the best-fit lines (parabolas) according to the red dots in the first 11 (last 8) plots.



1186
 1187
 1188
 1189
 1190
 1191
 1192

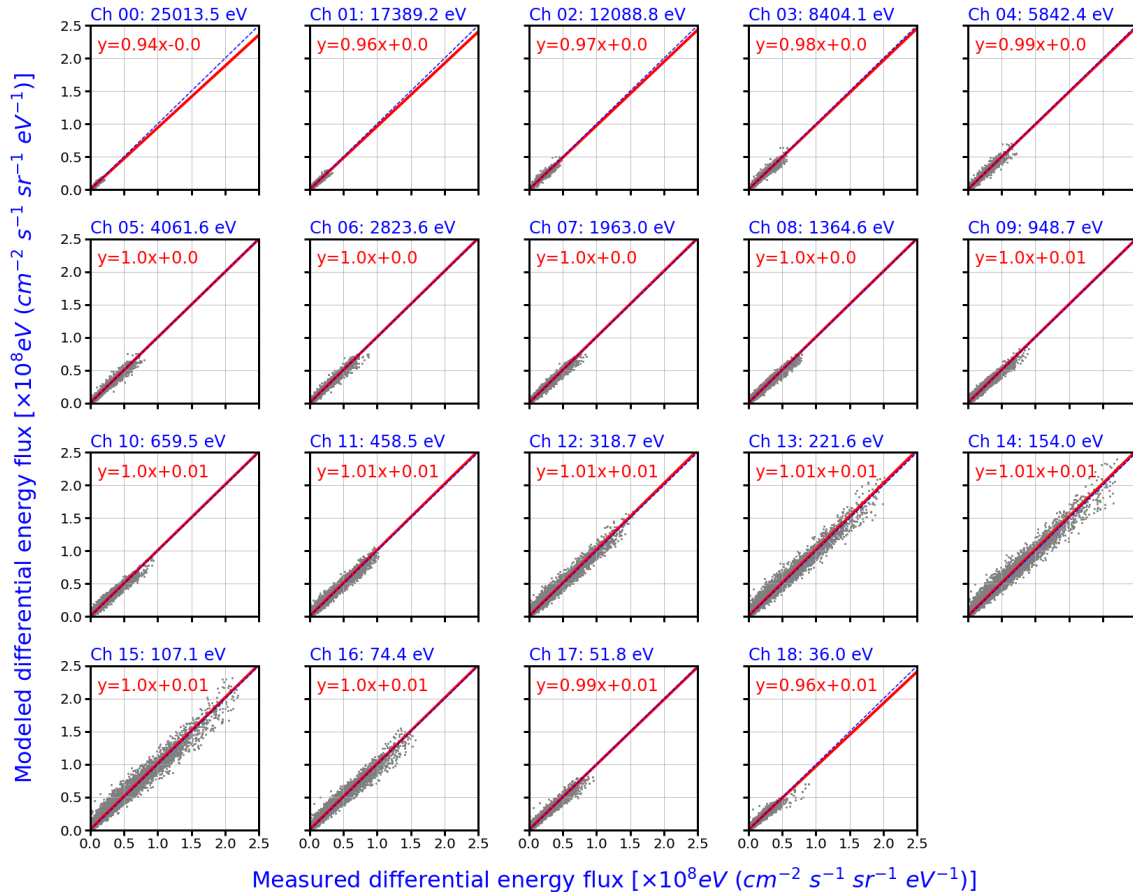
Figure 2. The cross-polar-cap potentials (CPCPs) from all 6 ϵ_t - θ_c bins for the ASHLEY-E development where θ_c is centered at 180° . The red thick line represents the best-fit curve according to the blue circles.



1193
 1194
 1195
 1196
 1197
 1198
 1199
 1200
 1201
 1202
 1203
 1204

Figure 3. (a) Evolution of the averaged co-MLATs of the poleward auroral boundary (PAB) identified on the dawn (4-8 MLT) and dusk (16-20 MLT) sides along the same polar crossing as a function of ε_t when $157.5^\circ < \theta_c < 202.5^\circ$. (b) Evolution of the averaged co-MLATs of the convection reversal boundary (CRB) identified on the dawn (4-8 MLT) and dusk (16-20 MLT) sides along the same polar crossing as a function of ε_t when $157.5^\circ < \theta_c < 202.5^\circ$. The red-thick line in each plot indicates the best-fit curve according to the black dots. (MLAT=magnetic latitude)

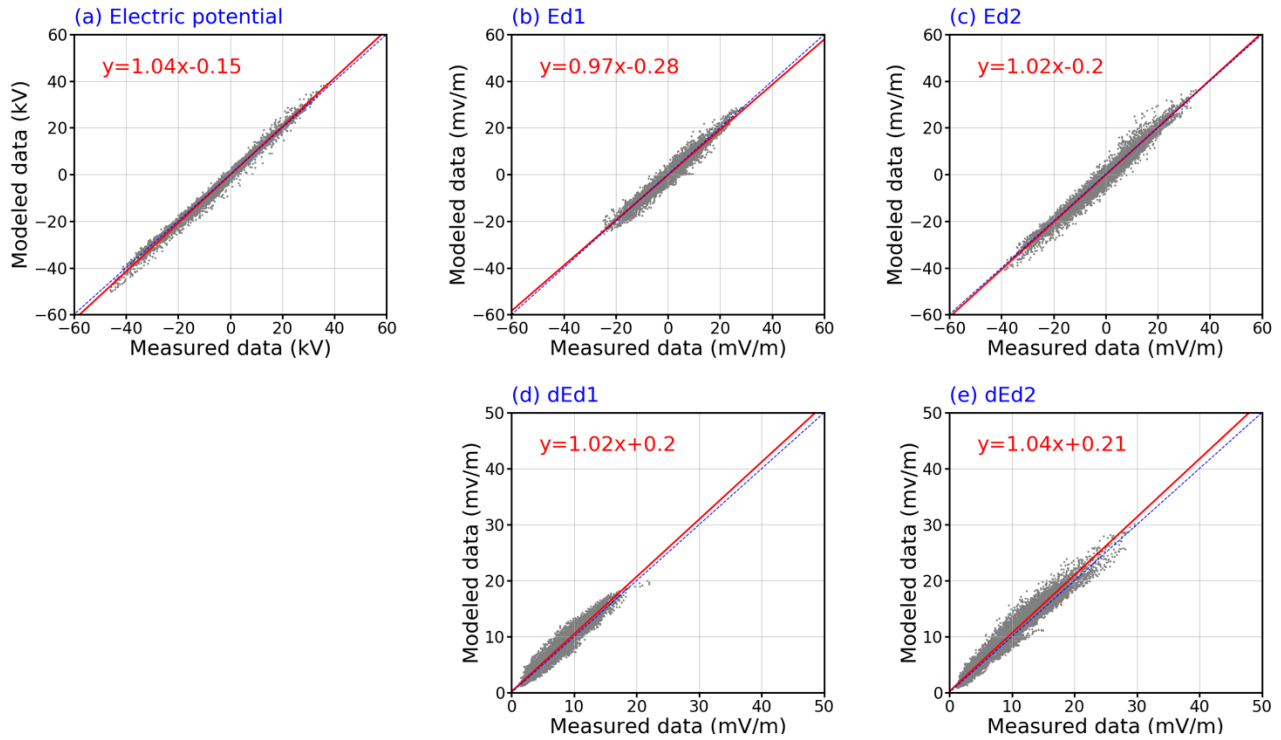
1205



1206
 1207
 1208
 1209
 1210
 1211
 1212
 1213
 1214
 1215

Figure 4. Comparisons of the averages of measured and modeled differential energy fluxes from all MLT-MLAT and ε_t - θ_c bins in the 19 DMSP energy channels. The numbers of the MLT, MLAT and ε_t - θ_c bin are 24, 40 (50° - 90° MLAT) and 65, respectively. The blue dashed line in each plot denotes the $y = x$ line, and the red thick line indicates the best-fit line according to the grey dots. The equation of the best-fit line is given in each plot.

1216

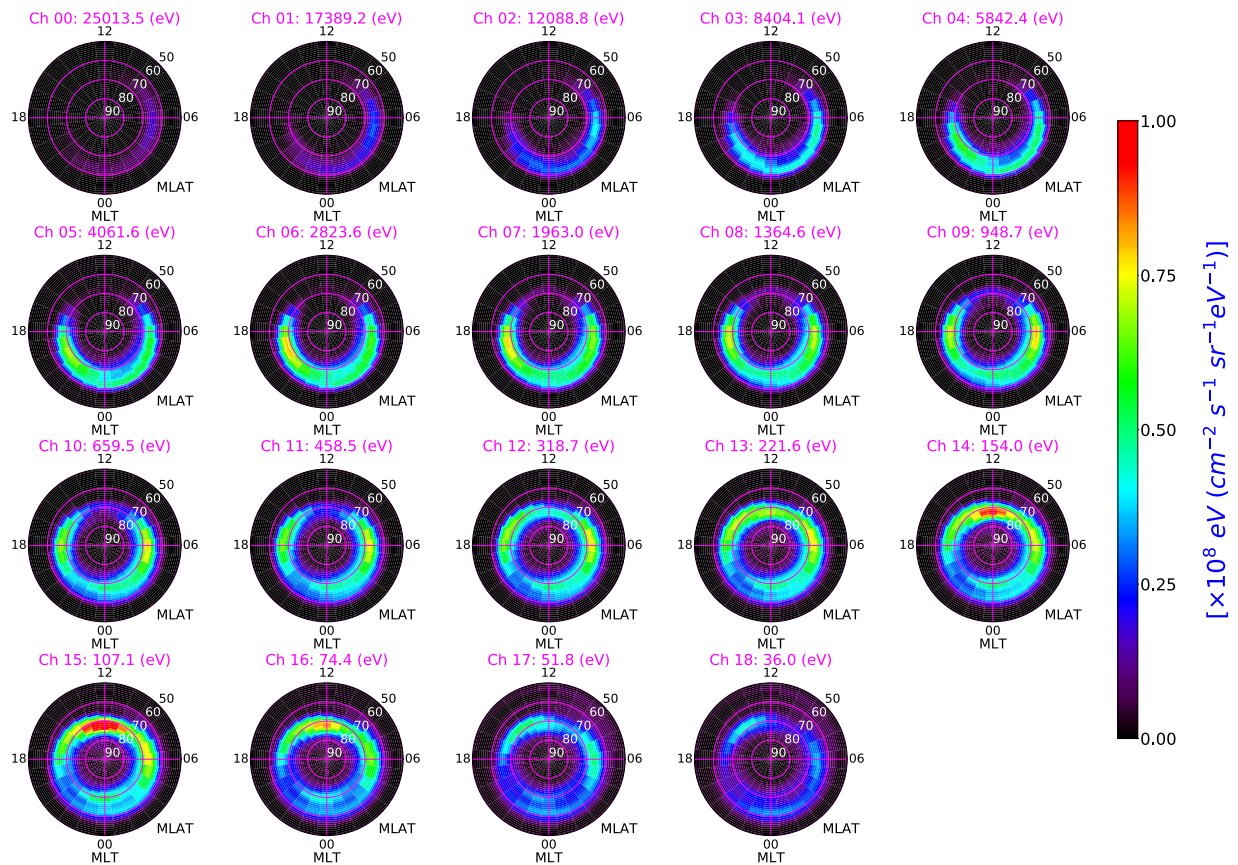


1217
1218

1219 Figure 5. (Top) Comparisons of the averages of measured and modeled (a) electric potential, (b)
1220 E_{d1} and (c) E_{d2} from all MLT-MLAT and $\varepsilon_t - \theta_c$ bins. (Bottom) Comparisons of (d) the standard
1221 deviation of measured E_{d1} and the root mean square (RMS) of modeled E_{d1} variability along with
1222 (e) the standard deviation of measured E_{d2} and the RMS of modeled E_{d2} variability from all
1223 MLT-MLAT and $\varepsilon_t - \theta_c$ bins. The numbers of the MLT, MLAT and $\varepsilon_t - \theta_c$ bin are 24, 20 ($50^\circ - 90^\circ$
1224 MLAT) and 49, respectively. The blue dashed line in each plot denotes the $y = x$ line, and the red
1225 thick line represents indicate the best-fit line according to the grey dots. The equation of the best-
1226 fit line is given in each plot.

1227
1228

1229



1230

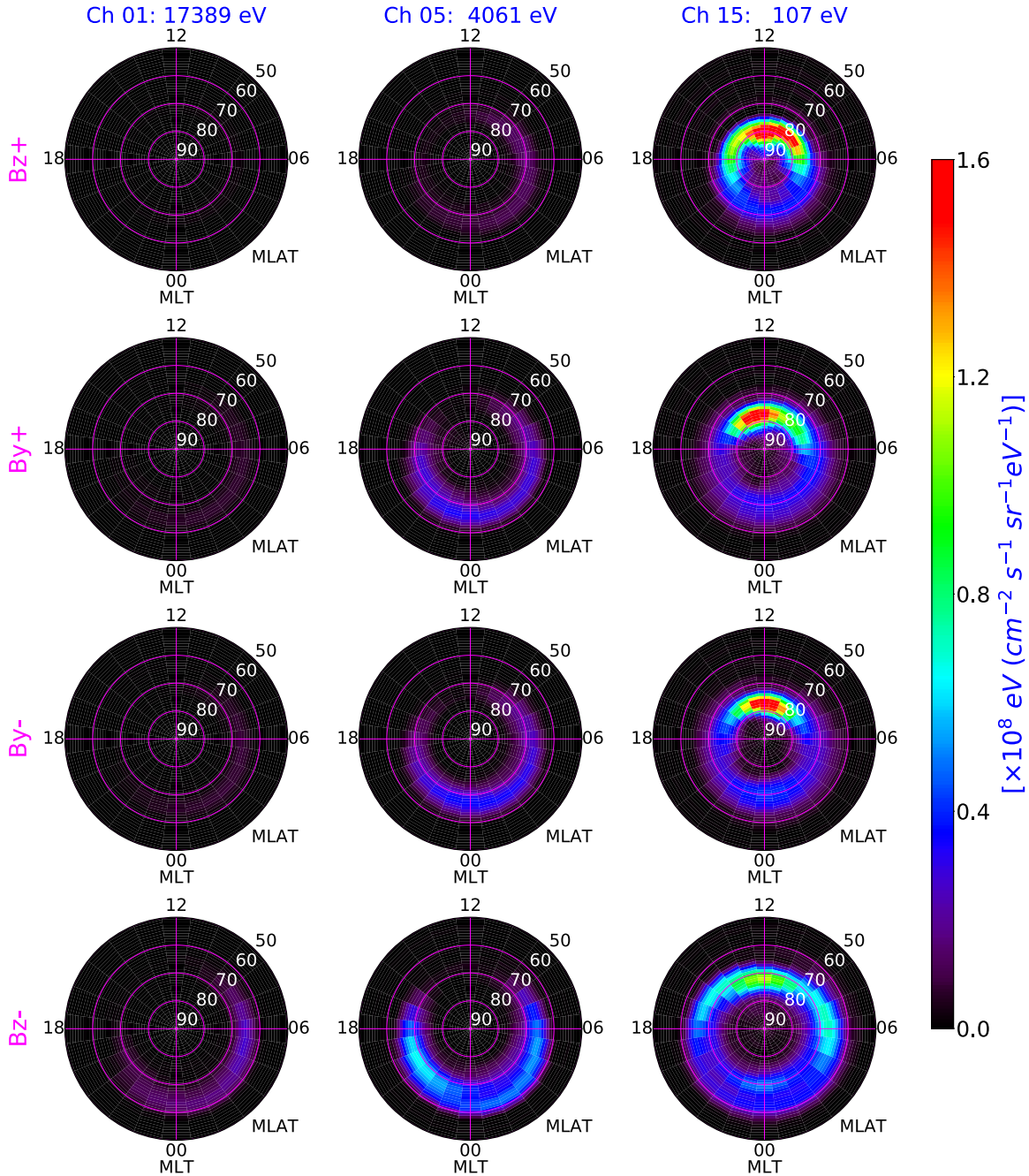
1231

1232 Figure 6. Distributions of the differential energy flux in the 19 DMSP energy channels as a
1233 function of MLT and MLAT (IMF $B_y = 0$, IMF $B_z = -8$ nT, $V_{SW} = 450$ km/s and $N_{SW} = 5$ cm⁻³).

1234 All plots are presented in geomagnetic coordinates. (DMSP: Defense Meteorological Satellite
1235 Program; MLT=magnetic local time; MLAT=magnetic latitude; IMF=interplanetary magnetic
1236 field)

1237

1238

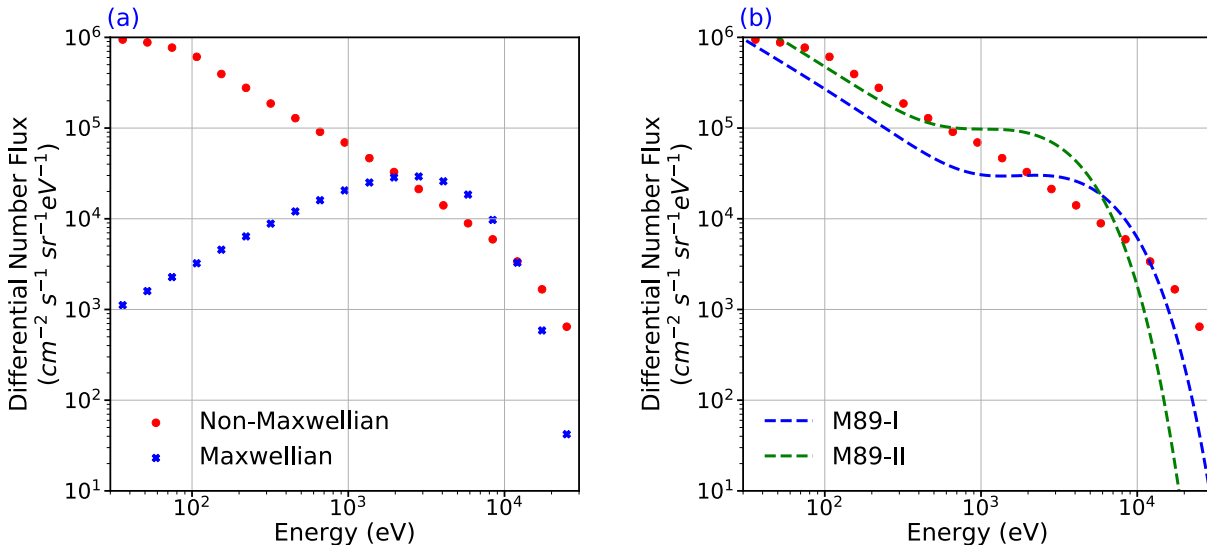


1239
1240

1241 Figure 7. Distributions of the differential energy flux in 3 selected DMSP energy channels as a
 1242 function of MLAT and MLT when the IMF is purely northward, downward, duskward and
 1243 southward (from top to bottom). For these four cases, the IMF and solar wind conditions are:
 1244 IMF $B_T = 8$ nT, $V_{SW} = 450$ km/s and $N_{SW} = 5$ cm^{-3} . All plots are presented in geomagnetic
 1245 coordinates. (DMSP: Defense Meteorological Satellite Program; MLT=magnetic local time;
 1246 MLAT=magnetic latitude; IMF=interplanetary magnetic field)

1247
1248
1249

1250



1251

1252

1253

1254

1255

1256

1257

1258

1259

1260

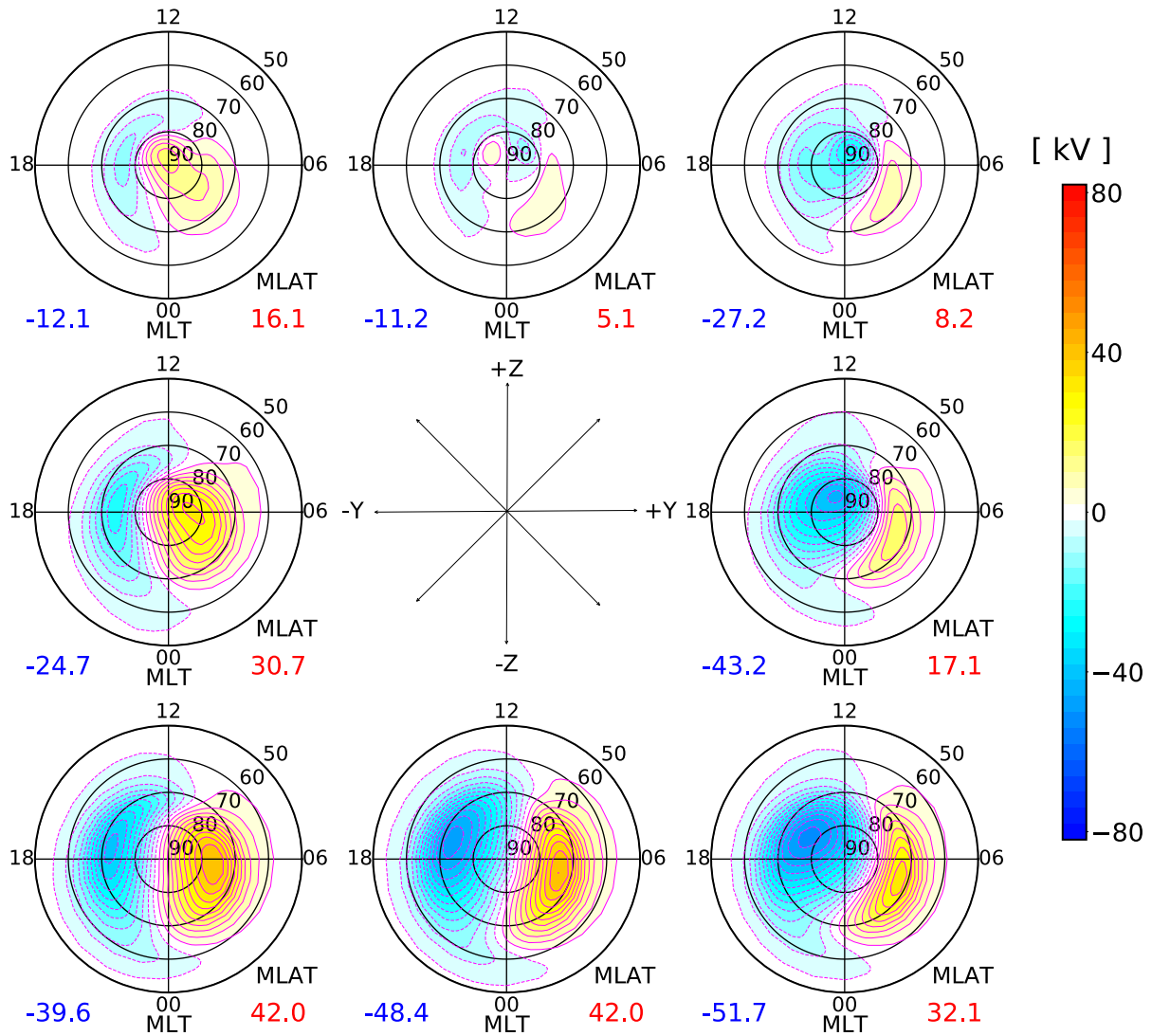
1261

1262

1263

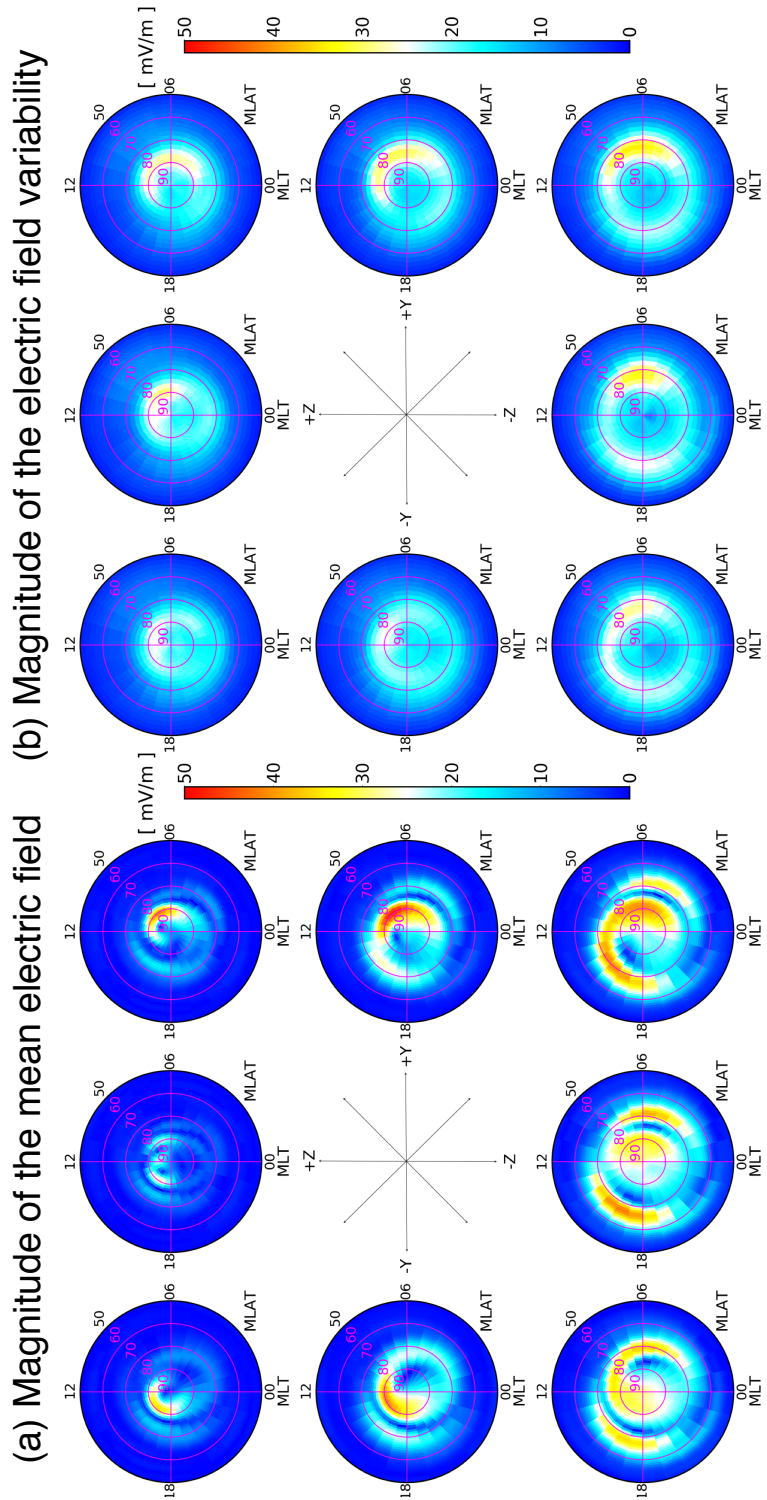
1264

Figure 8 (a) Comparisons of the differential number fluxes between the modeled spectrum (Red dots) and a Maxwellian spectrum (Blue crosses) derived from the total energy flux and average energy of the >500 eV portion of the modeled spectrum. (b) Comparisons of the differential number fluxes between the modeled spectrum (Red dots) and two spectra calculated by using the Meier 1989 formula (blue and green dashed lines). The blue and green dashed lines indicate the spectra calculated by using the total energy flux and average energy of the >500 eV portion of the modeled spectrum and the whole modeled spectrum, respectively. The location is at $\text{MLT}=4.5$ h and $\text{MLAT}=64.5^\circ$. The IMF and solar wind conditions are: $\text{IMF } B_y = 0$, $\text{IMF } B_z = -8$ nT, $V_{\text{sw}} = 450$ km/s and $N_{\text{sw}} = 5 \text{ cm}^{-3}$. (MLT=magnetic local time; MLAT=magnetic latitude; IMF=interplanetary magnetic field)



1265
 1266
 1267
 1268
 1269
 1270
 1271
 1272
 1273
 1274
 1275

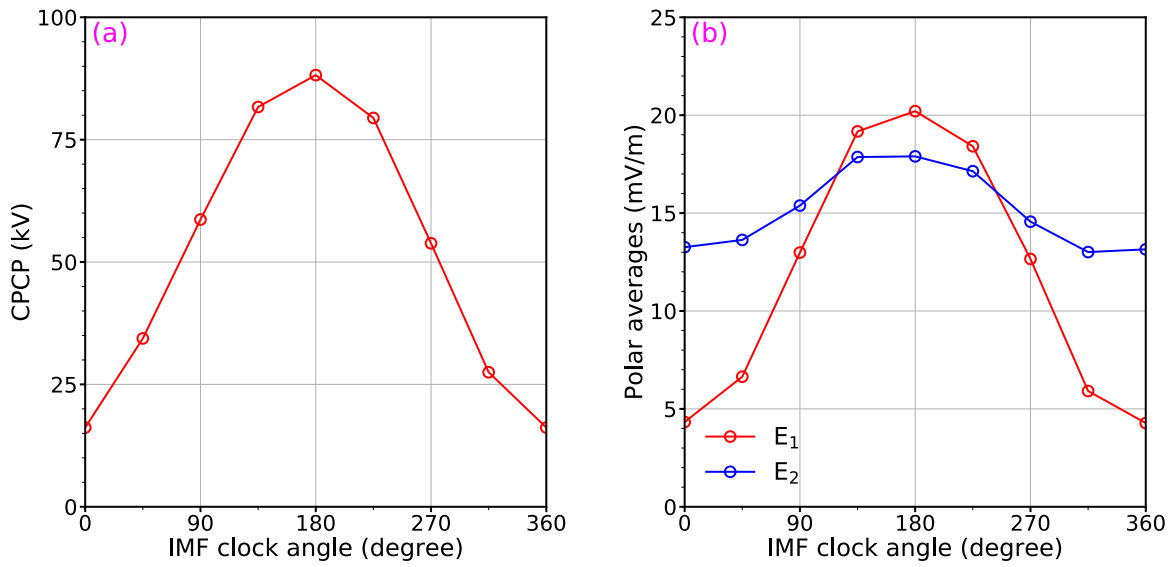
Figure 9. High-latitude electric potential outputs of ASHLEY-E at eight different IMF clock angles as a function of MLAT and MLT. For the cases shown in this figure, the solar wind and IMF conditions are: IMF $B_T = 8$ nT, $V_{SW} = 450$ km/s and $N_{SW} = 5$ cm⁻³. The maximum and minimum electric potential of each case are indicated on the bottom left and right sides of each plot, respectively, and the contour interval is 4 kV. All plots are presented in geomagnetic coordinates. (IMF=interplanetary magnetic field)



1276
 1277
 1278
 1279
 1280
 1281
 1282

Figure 10. Distributions of the (a) mean electric field and (b) electric field variability magnitudes as a function of MLAT and MLT for eight different IMF clock angles. For the cases shown here, the IMF and solar wind conditions are: IMF $B_T = 8$ nT, $V_{SW} = 450$ km/s and $N_{SW} = 5$ cm⁻³. All plots are presented in geomagnetic coordinates. (MLT=magnetic local time; MLAT=magnetic latitude; IMF=interplanetary magnetic field)

1283



1284

1285

1286

1287

1288

1289

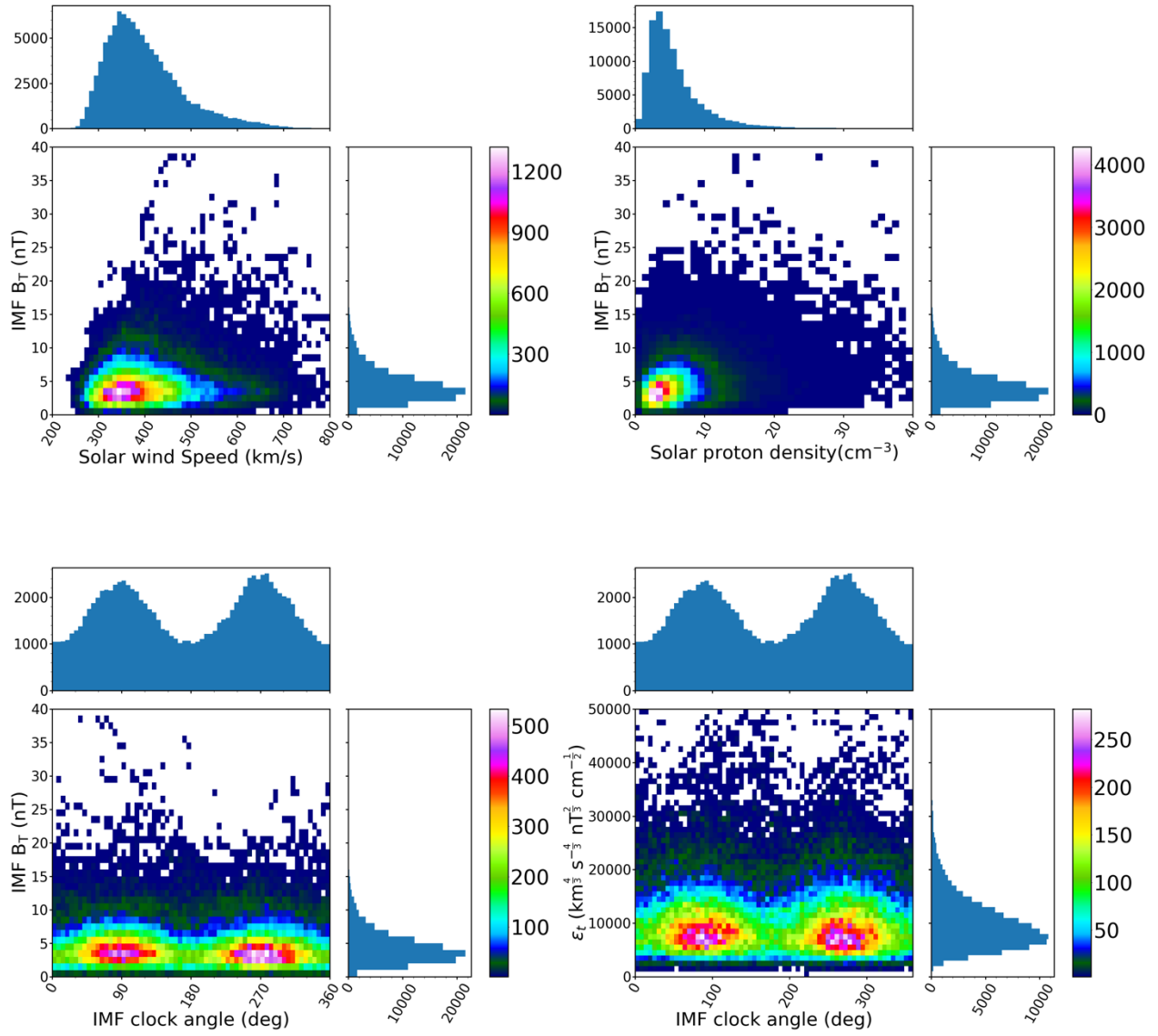
1290

1291

1292

1293

Figure 11. (a) Variation of the cross-polar-cap potential (CPCP) with respect to the IMF clock angle; (b) Variations of the averages of the mean electric field magnitude (E_1 , red) and electric field variability magnitude (E_2 , blue) over the region where $|\text{MLAT}| > 60^\circ$ as a function of the IMF clock angle. For the cases shown here, the IMF and solar wind conditions are: IMF $B_T = 8$ nT, $V_{SW} = 450$ km/s and $N_{SW} = 5$ cm^{-3} . (MLAT=magnetic latitude; IMF=interplanetary magnetic field)

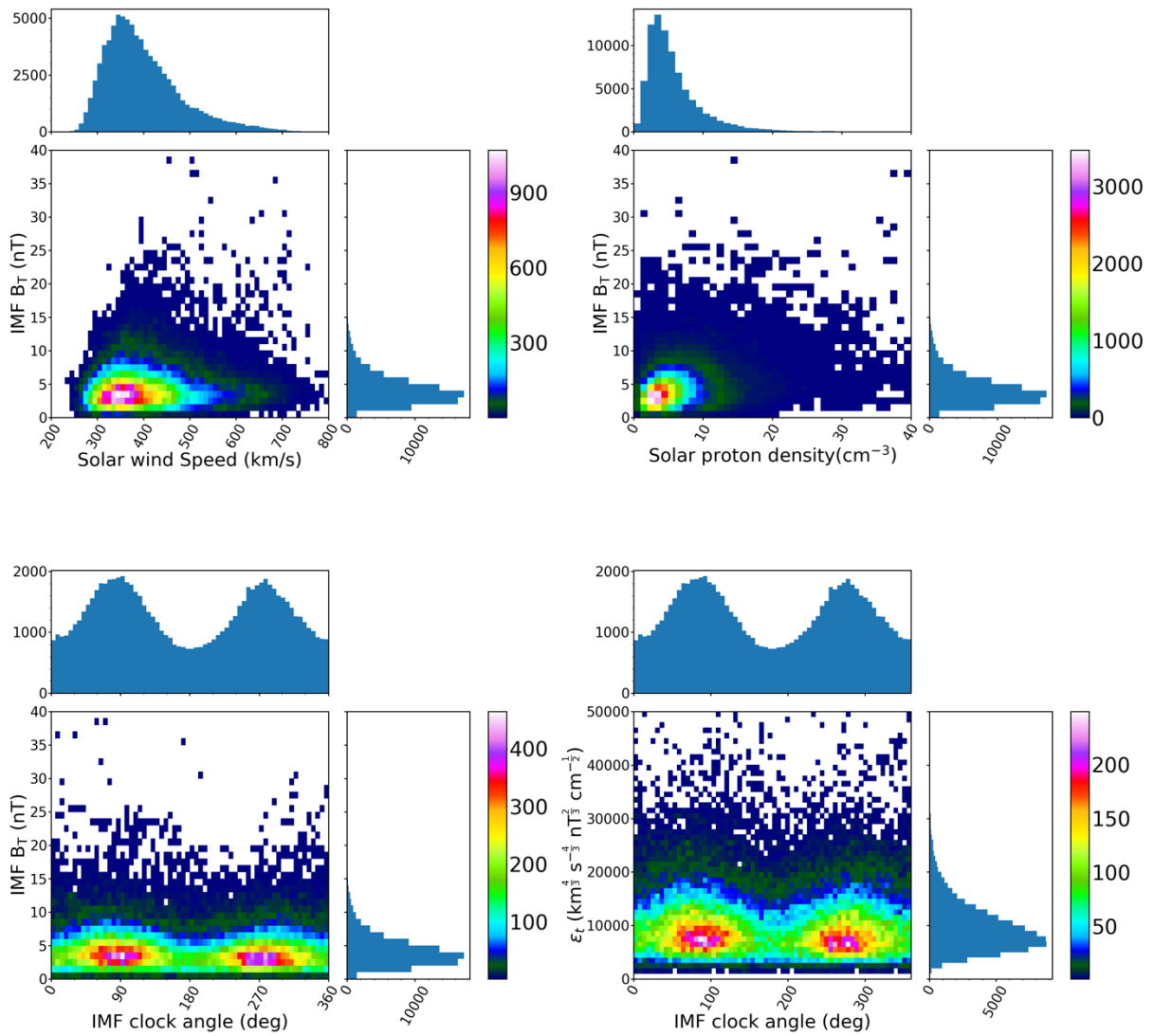


1294

1295 **Figure S1.** Distributions of the IMF and solar wind data used for the ASHLEY-A development.

1296

1297

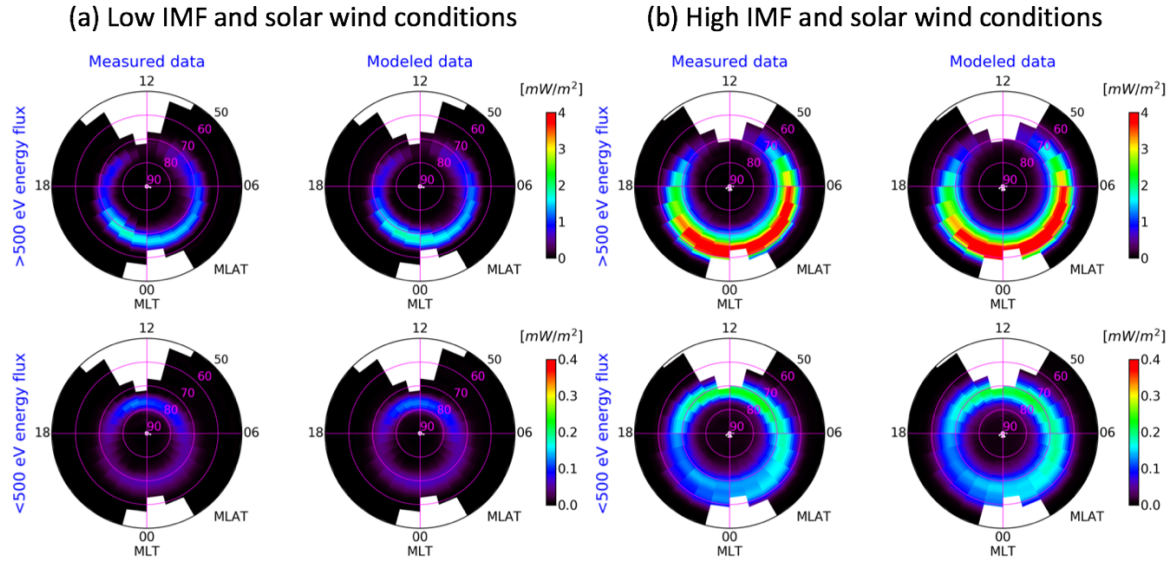


1298

1299 **Figure S2.** Distributions of the IMF and solar wind data used for the ASHLEY-E and ASHLEY-
 1300 Evar developments.

1301

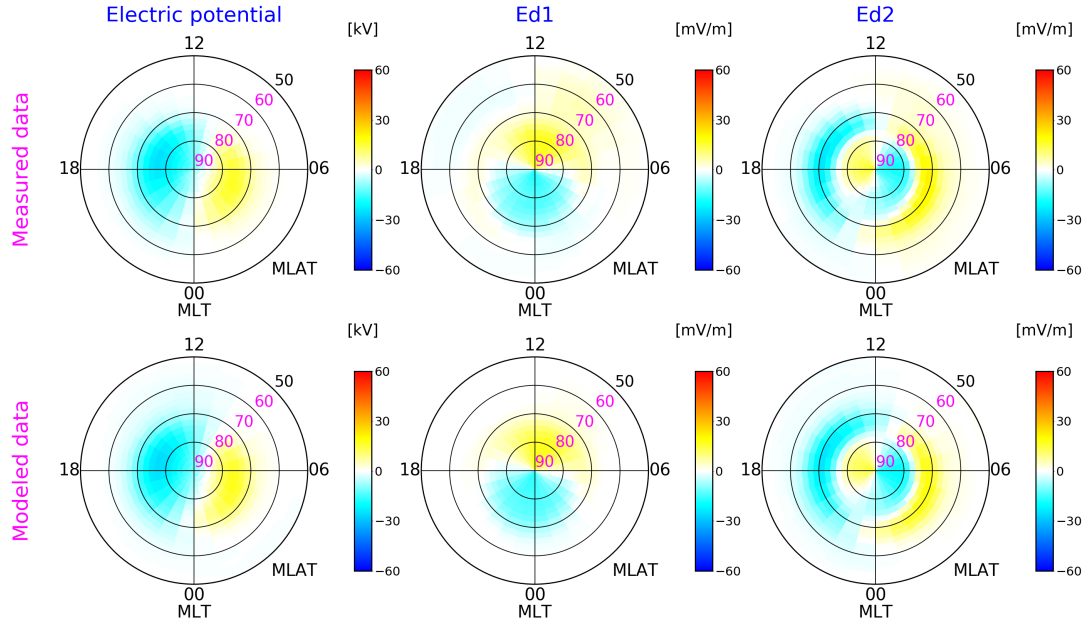
1302



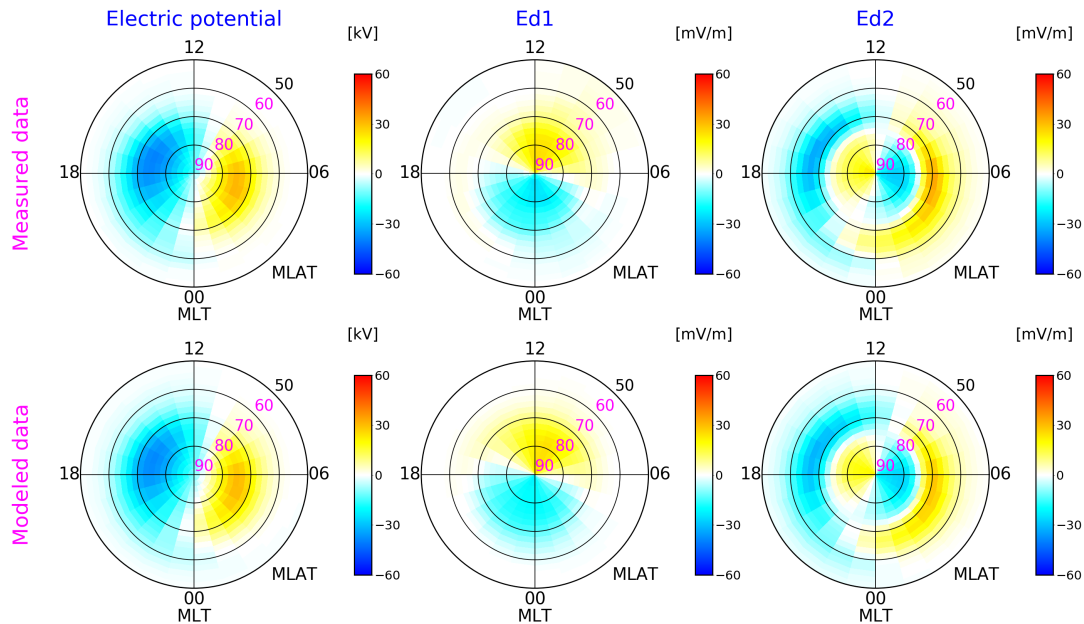
1303
 1304
 1305
 1306
 1307
 1308
 1309
 1310
 1311

Figure S3. Comparisons of averages of the measured and modeled integrated differential energy fluxes in different MLAT-MLT bins under (a) low IMF and solar wind conditions ($5000 \leq \varepsilon_t < 7000$, $157.5^\circ < \theta_c < 202.5^\circ$) and (b) high IMF and solar wind conditions ($20000 \leq \varepsilon_t < 30000$, $112.5^\circ < \theta_c < 157.5^\circ$). The parameters shown in the top and bottom row of each plot are the integrated differential energy fluxes of >500 eV and <500 eV electrons, respectively. All plots are presented in geomagnetic coordinates.

(a) Low IMF and solar wind conditions

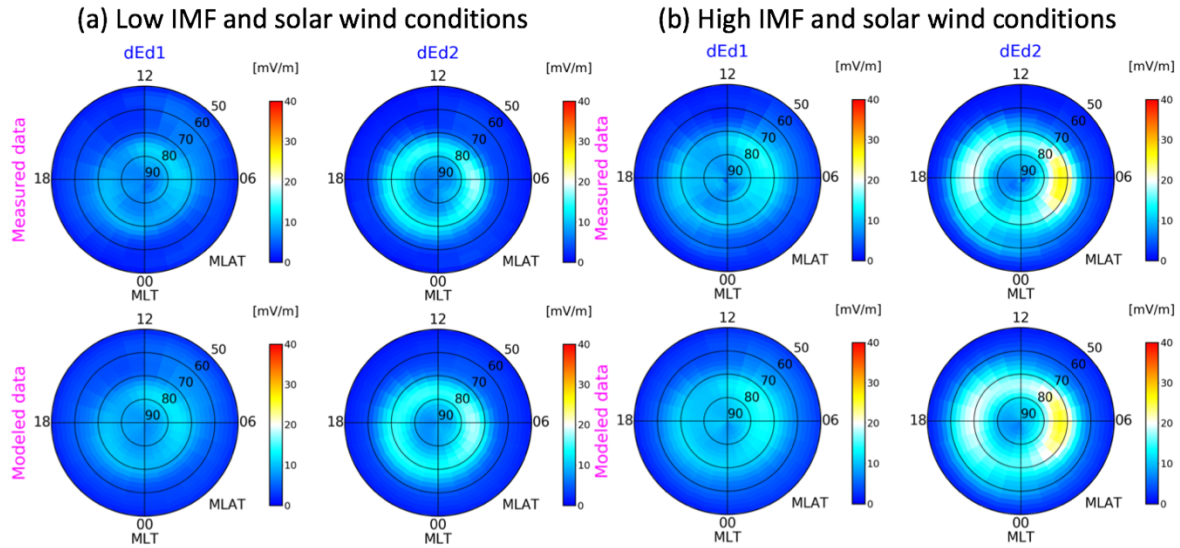


(b) High IMF and solar wind conditions



1312
1313
1314
1315
1316
1317
1318

Figure S4. Comparisons of averages of the measured and modeled electric potential, E_{d1} and E_{d2} in different MLAT-MLT bins under (a) low IMF and solar wind conditions ($5500 \leq \epsilon_t < 7500$, $157.5^\circ < \theta_c < 202.5^\circ$) and (b) high IMF and solar wind conditions ($12000 \leq \epsilon_t < 16000$, $157.5^\circ < \theta_c < 202.5^\circ$). Here, E_{d1} and E_{d2} are magnetic eastward and northward components of the electric field, respectively. All plots are presented in geomagnetic coordinates.



1319
 1320
 1321
 1322
 1323
 1324
 1325
 1326
 1327
 1328
 1329
 1330

Figure S5. Comparisons of the standard deviations of measured E_{d1} and E_{d2} and the root mean squares (RMSs) of modeled E_{d1} and E_{d2} variabilities in different MLAT-MLT bins under (a) low IMF and solar wind conditions ($5500 \leq \epsilon_t < 7500$, $157.5^\circ < \theta_c < 202.5^\circ$) and (b) high IMF and solar wind conditions ($12000 \leq \epsilon_t < 16000$, $157.5^\circ < \theta_c < 202.5^\circ$). Here, E_{d1} and E_{d2} are magnetic eastward and northward components of the electric field, respectively. All plots are presented in geomagnetic coordinates.